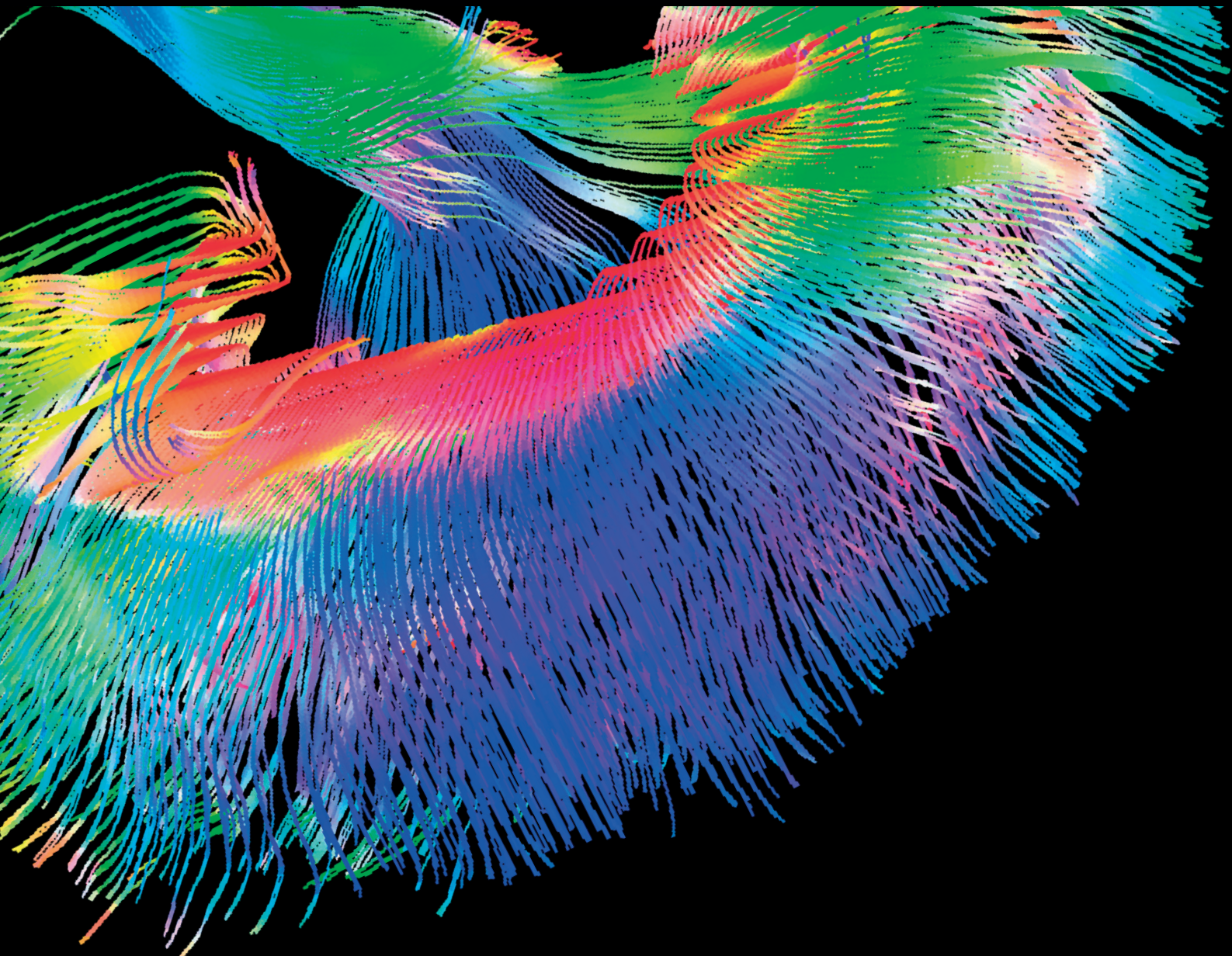


Contrast Media & Molecular Imaging

Application of Image Processing Techniques in Molecular Imaging of Cancer

Lead Guest Editor: Bingsheng Huang

Guest Editors: Shengxian Rao, Guoyan Zheng, Ziyue Xu, and Silun Wang





Application of Image Processing Techniques in Molecular Imaging of Cancer

Contrast Media & Molecular Imaging

Application of Image Processing Techniques in Molecular Imaging of Cancer

Lead Guest Editor: Bingsheng Huang

Guest Editors: Shengxian Rao, Guoyan Zheng, Ziyue Xu,
and Silun Wang



Copyright © 2017 Hindawi. All rights reserved.

This is a special issue published in “Contrast Media & Molecular Imaging.” All articles are open access articles distributed under the Creative Commons Attribution License, which permits unrestricted use, distribution, and reproduction in any medium, provided the original work is properly cited.

Editorial Board

Peter Bannas, Germany
Giorgio Biasiotto, Italy
Dinesh K. Deelchand, USA
Françoise Kraeber-Bodéré, France
Gaurav Malviya, UK
Isabelle Miederer, Germany

Barbara Palumbo, Italy
Giancarlo Pascali, Australia
Maria Joao Ribeiro, France
Anne Roivainen, Finland
Pedro Rosa-Neto, Canada
Giuseppe Rubini, Italy

Barbara Salvatore, Italy
Ralf Schirmacher, Canada
Fijs W. B. Van Leeuwen, Netherlands
Luc Zimmer, France

Contents

Application of Image Processing Techniques in Molecular Imaging of Cancer

Bingsheng Huang, Guoyan Zheng, Ziyue Xu, Shengxiang Rao, and Silun Wang
Volume 2017, Article ID 2758749, 2 pages

Application of Deep Learning in Automated Analysis of Molecular Images in Cancer: A Survey

Yong Xue, Shihui Chen, Jing Qin, Yong Liu, Bingsheng Huang, and Hanwei Chen
Volume 2017, Article ID 9512370, 10 pages

Head and Neck Cancer Tumor Segmentation Using Support Vector Machine in Dynamic Contrast-Enhanced MRI

Wei Deng, Liangping Luo, Xiaoyi Lin, Tianqi Fang, Dexiang Liu, Guo Dan, and Hanwei Chen
Volume 2017, Article ID 8612519, 5 pages

PET Imaging of FSHR Expression in Tumors with ⁶⁸Ga-Labeled FSH1 Peptide

Donghui Pan, Guifeng Liu, Yuping Xu, Yanting Wang, Yuanyuan Yue, Lizhen Wang, Junjie Yan, Xinyu Wang, Runlin Yang, and Min Yang
Volume 2017, Article ID 2674502, 8 pages

An Individually Optimized Protocol of Contrast Medium Injection in Enhanced CT Scan for Liver Imaging

Shi-Ting Feng, Hongzhang Zhu, Zhenpeng Peng, Li Huang, Zhi Dong, Ling Xu, Kun Huang, Xufeng Yang, Zhi Lin, and Zi-Ping Li
Volume 2017, Article ID 7350429, 8 pages

Dynamic Contrast-Enhanced Magnetic Resonance Imaging of Regional Nodal Metastasis in Nasopharyngeal Carcinoma: Correlation with Nodal Staging

Bingsheng Huang, Dora Lai-Wan Kwong, Vincent Lai, Queenie Chan, Brandon Whitcher, and Pek-Lan Khong
Volume 2017, Article ID 4519653, 6 pages

Editorial

Application of Image Processing Techniques in Molecular Imaging of Cancer

Bingsheng Huang,¹ Guoyan Zheng,² Ziyue Xu,³ Shengxiang Rao,⁴ and Silun Wang⁵

¹*School of Biomedical Engineering, Health Science Centre, Shenzhen University, Shenzhen, China*

²*Institute for Surgical Technology and Biomechanics, University of Bern, Bern, Switzerland*

³*Center for Infectious Disease Imaging (CID), Radiology and Imaging Science Department, National Institutes of Health (NIH), Bethesda, MD 20892, USA*

⁴*Department of Radiology, Zhongshan Hospital, Fudan University, Shanghai, China*

⁵*Department of Radiology and Imaging Sciences, Emory University School of Medicine, Atlanta, GA, USA*

Correspondence should be addressed to Bingsheng Huang; huangbs@gmail.com

Received 23 October 2017; Accepted 23 October 2017; Published 13 November 2017

Copyright © 2017 Bingsheng Huang et al. This is an open access article distributed under the Creative Commons Attribution License, which permits unrestricted use, distribution, and reproduction in any medium, provided the original work is properly cited.

Cancer is one of the leading causes of death all over the world. The research of cancer has always been a major focus in the medical imaging field. Modern imaging technology such as molecular imaging has already been shown to be useful in enhancing cancer management, including early detection, more accurate diagnosis, better treatment planning, and treatment monitoring in an early stage. Molecular imaging enables *in vivo* visualization and measurement of biological process at the cellular and molecular level. It allows not only localization of tumor lesions but also visualization of the expression and activity of specific molecules, which have great influence on tumor behavior and response to treatment. Many different modalities, such as MRI, SPECT, and PET, have been developed and used for noninvasive molecular imaging and have played a critical role in clinical oncology. However, due to large intersubject variability and various parameters in molecular images, it is generally infeasible to derive a single analytic method or simple equations that can describe the targets such as lesions and anatomies in all the images. Hence, in order to facilitate further the application of molecular imaging in clinical oncology, image processing techniques have been widely applied to the detection of cancer, characterization and segmentation of tumor lesions, planning of cancer treatment, evaluation of the effectiveness of treatment, prognostication of cancer, and so forth. Therefore, advanced image processing techniques have become a major focus in molecular imaging research, so that we can

make better use of the rich information in the molecular image data.

The aim of this special issue is to provide a platform for high quality works on image processing and molecular imaging of cancer. Original papers and review articles focusing on the latest application of image processing techniques in multimodality cancer molecular imaging were submitted. The topics included pharmacokinetic modeling approaches, computer-aided detection/diagnosis of cancer, treatment evaluation and prognostication of cancer, segmentation/delineation of tumor lesions, correlation between molecular image data and other medical data of cancer from a medical perspective, advantages and limitations of existing and new imaging processing software/techniques, the importance of molecular image processing within the entire cycle of cancer patient management, and some other image processing techniques applied in cancer molecular imaging. We received a total of 16 submissions, and after two rounds of rigorous review, 5 papers were accepted for publications in this special issue.

In the paper “Head and Neck Cancer Tumor Segmentation Using Support Vector Machine in Dynamic Contrast-Enhanced MRI,” W. Deng et al. proposed an automatic method based on Support Vector Machine (SVM) and Dynamic Contrast-Enhanced Magnetic Resonance Imaging (DCE-MRI) to segment the tumor lesions of head and neck cancer (HNC). They calculated five curve features and

two principal components of the normalized time-intensity curve (TIC) and trained three SVM classifiers. Compared to similar studies in literature, their method has achieved higher accuracy, and the average area overlap measure (AOM) with the testing dataset was 0.76 ± 0.08 . This proposed method is of potential in the clinical practice for HNC.

In the paper "PET Imaging of FSHR Expression in Tumors with ^{68}Ga -Labeled FSHI Peptide," D. Pan et al. developed ^{68}Ga labeled FSHI peptide for imaging of FSHR in cancers. ^{68}Ga -NOTA-MAL-FSHI was produced within 20 min and the radiochemical purity was greater than 95%. In vitro studies and MicroPET imaging were performed in PC-3 prostate tumor model. It showed that ^{68}Ga -NOTA-MAL-FSHI possessed FSHR binding affinities. The tracer was stable in human serum for at least 2 hours. MicroPET imaging revealed that the PC-3 xenografts were clearly visualized. FSHR binding specificity was also demonstrated by reduced tumor uptake of ^{68}Ga -NOTA-MAL-FSHI after coinjecting excess unlabeled FSHI peptide. The favorable characters of ^{68}Ga -NOTA-MAL-FSHI such as convenient synthesis and specific tumor uptake warrant its further investigation for FSHR expression imaging.

In the paper "An Individually Optimized Protocol of Contrast Medium Injection in Enhanced CT Scan for Liver Imaging," S.-T. Feng et al. investigated the effectiveness of a new individualized contrast medium injection protocol for enhanced liver CT scan. Patients who underwent plain and dual phase enhanced liver CT were randomly assigned to 2 groups, one with individualized contrast medium injection protocol and the other with standard contrast medium injection. The mean contrast medium dose was statistically lower with the individualized protocol. There were no significant differences in CT values and ΔHU (CT value difference between plain and enhanced CT) of liver parenchyma and tumor-liver contrast between two groups. Two independent radiologists were in substantial conformity in grading tumor conspicuity. The authors concluded that using the individually optimized injection protocol might reduce contrast medium dose without impacting on the imaging quality in enhanced liver CT.

In the paper "Dynamic Contrast-Enhanced Magnetic Resonance Imaging of Regional Nodal Metastasis in Nasopharyngeal Carcinoma: Correlation with Nodal Staging," B. Huang et al. determined if the perfusion parameters by DCE-MRI of regional nodal metastasis were helpful in characterizing nodal status and to understand the relationship with those of primary tumor of nasopharyngeal carcinoma (NPC). 26 newly diagnosed patients with enlarged retropharyngeal/cervical lymph nodes suggestive of nodal disease were recruited and DCE-MRI was performed. Three quantitative parameters, K^{trans} , v_e , and k_{ep} , were calculated for the largest node in each patient and analyzed. K^{trans} was significantly different among the patients of N stages. There was no significant correlation between the parameters in nodes and primary tumors. The authors concluded that DCE-MRI may play a distinct role in characterizing the metastatic cervical lymph nodes of NPC.

In the review article "Application of Deep Learning in Automated Analysis of Molecular Images in Cancer: A Survey," Y. Xue et al. review the applications of deep learning in molecular imaging in terms of tumor lesion segmentation, tumor classification, and survival prediction. They also outline some future directions in which researchers may develop more powerful deep learning models for better performance in the applications in cancer molecular imaging.

Acknowledgments

The guest editorial team would like to thank the authors submitting their works to this special issue. The editors also thank the professional reviewers for their precious help with review assignments. They hope the papers of this special issue contribute to this interesting and fast-moving field of molecular imaging.

Bingsheng Huang
Guoyan Zheng
Ziyue Xu
Shengxiang Rao
Silun Wang

Review Article

Application of Deep Learning in Automated Analysis of Molecular Images in Cancer: A Survey

Yong Xue,^{1,2} Shihui Chen,³ Jing Qin,⁴ Yong Liu,⁵ Bingsheng Huang,^{2,3} and Hanwei Chen^{1,2}

¹Guangzhou Panyu Central Hospital, Guangzhou, China

²Medical Imaging Institute of Panyu, Guangzhou, China

³National-Regional Key Technology Engineering Laboratory for Medical Ultrasound, Guangdong Key Laboratory for Biomedical Measurements and Ultrasound Imaging, School of Biomedical Engineering, Health Science Centre, Shenzhen University, Shenzhen, China

⁴School of Nursing, The Hong Kong Polytechnic University, Hung Hom, Hong Kong

⁵Intensive Care Unit, Southern Medical University Shenzhen Hospital, Shenzhen, China

Correspondence should be addressed to Bingsheng Huang; huangbs@gmail.com and Hanwei Chen; docterwei@sina.com

Received 7 April 2017; Accepted 6 September 2017; Published 15 October 2017

Academic Editor: Ralf Schirmacher

Copyright © 2017 Yong Xue et al. This is an open access article distributed under the Creative Commons Attribution License, which permits unrestricted use, distribution, and reproduction in any medium, provided the original work is properly cited.

Molecular imaging enables the visualization and quantitative analysis of the alterations of biological procedures at molecular and/or cellular level, which is of great significance for early detection of cancer. In recent years, deep learning has been widely used in medical imaging analysis, as it overcomes the limitations of visual assessment and traditional machine learning techniques by extracting hierarchical features with powerful representation capability. Research on cancer molecular images using deep learning techniques is also increasing dynamically. Hence, in this paper, we review the applications of deep learning in molecular imaging in terms of tumor lesion segmentation, tumor classification, and survival prediction. We also outline some future directions in which researchers may develop more powerful deep learning models for better performance in the applications in cancer molecular imaging.

1. Introduction

With increasing incidence and mortality, cancer has always been a leading cause of death for many years. According to American Cancer Society, there are around 1,685,210 new cases and 595,690 deaths in 2016 [1]. It was reported that the 5-year survival rate for the cancer patients diagnosed in early stage was as high as 90% [2]. In this regard, early and precise diagnosis is critical for better prognosis of cancer.

Molecular imaging is an imaging technique to visualize, characterize, and measure biological procedures at molecular and/or cellular level [3] and has been considered as a powerful tool for early detection of cancer. Compared with anatomical imaging techniques, molecular imaging is more promising in diagnosing cancer in the early stage, as it is capable of signaling the molecular or physiological alterations in cancer patients which may happen before the obvious

anatomical changes. Molecular imaging is also helpful in individualized therapy as it can reflect the treatment response at the molecular level. Therefore, molecular imaging has been widely used in cancer management.

The current molecular imaging modalities in clinical practice include contrast-enhanced computed tomography (CT), contrast-enhanced magnetic resonance (MR) imaging, MR spectroscopy, and nuclear medicine such as single photon emission computed tomography (SPECT) and positron emission tomography (PET). Visual assessment conducted by the radiologists is the most common way to analyze these images. However, subtle changes in molecular images may be difficult to detect by visual inspection as the target-to-background ratio in these images is not that significant. In addition, visual interpretation by clinicians not only is time-consuming but also usually causes large variations across interpreters due to the different experience.

The emerging intelligent techniques are of great potential in solving these problems by making the image interpretation automated. Machine learning-based image processing has been widely used in the domain of medical imaging analysis. Conventional machine learning techniques require the artificial intervention of feature extraction and selection and thus are still somehow subjective. In addition, the subtle and distributed changes may be ignored with artificial feature calculation and selection. Fully automated techniques are expected to integrate the local and global information for more accurate interpretation. Deep learning as a state-of-the-art machine learning technique may solve the challenges aforementioned by abstracting higher level features and improving the predictions from data with deep and complex neural network structures [4].

1.1. Deep Learning. The deep architectures and algorithms have been summarized [5, 6]. Compared with the conventional machine learning techniques, deep learning has shown some advantages [5, 6]. First, deep learning can automatically acquire much richer information in a data-driven manner and these features are usually more discriminative than the traditional hand-crafted features. Second, deep learning models are usually trained in an end-to-end way; thus the feature extraction, feature selection, and classification can be conducted and gradually improved through supervised learning in an interactive manner [7]. Therefore, deep learning is promising in a wide variety of applications including cancer detection and prediction based on molecular imaging, such as in brain tumor segmentation [8], tumor classification, and survival prediction. Deep learning-based automated analysis tools can greatly alleviate the heavy workload of radiologists and physicians caused by the popularity of molecular imaging in early diagnosis of cancer as well as enhance the diagnostic accuracy, especially when there exist subtle pathological changes that cannot be detected by visual assessment.

Deep learning-based methods mainly include convolutional neural networks (CNN), restricted Boltzmann machines (RBMs), autoencoder, and sparse coding [9]. Among them, CNN and autoencoder have been widely applied in cancer molecular imaging. To our best knowledge, CNN models are especially the most commonly used methods with more powerful architecture and flexible configuration to learn more discriminative features for more accurate detection [10]. A typical CNN architecture for image processing consists of three types of neural layers, including the convolutional layers, the pooling layers, and the fully connected layers. The convolutional layer contains a series of convolution filters, which can learn the features from training data through various kernels and generate various feature maps. A pooling layer is generally applied to reduce the dimension of feature maps and network parameters, and a fully connected layer is used to combine the feature maps as a feature vector for classification. Because the fully connected layers require a large computational effort during the training process, they are often replaced with convolutional layers to accelerate the training procedure [11, 12]. On the other hand, autoencoder is based on the reconstruction of its own inputs

and is optimized by minimizing the reconstruction error [9].

1.2. Literature Selection and Classification. The papers on diverse applications of deep learning in different molecular imaging of cancer published from 2014 onwards were included. This review contains 25 papers and is organized according to the application of deep learning in cancer molecular imaging, including tumor lesion segmentation, cancer classification, and prediction of patient survival. Table 1 summarizes the 13 different studies on tumor lesion segmentation, while Table 2 summarizes the 10 different studies on cancer classification. Two interesting papers on prediction of patient survival are also reviewed (Table 3). To our best knowledge, there is no previous work making such a comprehensive review on this issue. In this regard, we believe this survey can present radiologists and physicians with the application status of advanced artificial intelligent techniques in molecular images analysis and hence inspire more applications in clinical practice. Biomedical engineering researchers may also benefit from this survey by acquiring the state of the art in this field or inspiration for better models/methods in future research.

2. Deep Learning in Tumor Lesion Segmentation

Accurate tumor segmentation plays an essential role in treatment planning and the assessment of radiotherapy treatment efficacy. Studies have focused on tumor segmentation based on deep learning and molecular imaging, aiming at providing powerful tools for clinicians to automatically and accurately delineate lesions for better diagnosis and treatment.

Postcontrast T1W-MRI is a molecular imaging technique, which is of great help in delineating the enhancing lesions and necrotic regions. Indeed, deep learning models have been trained with multimodality MRI data, including contrast-enhanced T1W, to achieve better performance in brain tumor segmentation.

Deep neural networks (DNN) were found effective for task-specific high-level feature learning [13] and thus were used to detect MRI brain-pathology-specific features by integrating information from multimodal MRI. In four brain tumor patients, Zhou et al. [14] applied the incremental manifold learning [15] and DNN models to predict tumor progression, respectively. For incremental manifold learning system, feature extraction consists of three parts: landmark selection using statistical sampling methods, manifold skeleton identification from the landmarks, and inserting out-of-bag samples into the skeleton with Locally Linear Embedding (LLE) algorithm [16, 17]. Fisher score and Gaussian mixture model (GMM) were employed for feature selection and classifier training, respectively. For DNN, feature extraction, feature selection, and classification were achieved in the same deep model by pretraining the model in an unsupervised way and then fine-tuning the model parameters with label. Though the average result produced by deep neural network models was just a little better than that of the incremental

TABLE I: Comparison of the performance of different deep learning-based segmentation methods.

Publication	Type of images	Proposed methods		Comparison baseline	
		Method	Results	Method	Results
Zhou et al. [14]	Multiple MRI	DNN	average = 0.864 (average of SEN, SPE and PRE)	Manifold learning	Average = 0.849
Zikic et al. [19]	BRATS 2013	CNN	HGG (complete): ACC = 0.837 ± 0.094	RF	HGG: ACC = 0.763 ± 0.124
Lyksborg et al. [20]	Multimodal MRI	CNN	Dice = 0.810, PPV = 0.833, SEN = 0.825	Axially trained 2D network	Dice = 0.744, PPV = 0.732, SEN = 0.811
Dvořák and Menze [23]	BRATS 2014	CNN	HGG (complete): Dice = 0.83 ± 0.13	—	—
Pereira et al. [24]	BRATS 2015	CNN	LGG (complete): DSC = 0.86, PPV = 0.86, SEN = 0.88 HGG (complete): DSC = 0.87, PPV = 0.89, SEN = 0.86 Combined: DSC = 0.87, PPV = 0.89, SEN = 0.86	—	—
Pereira et al. [25]	BRATS 2013	CNN	DSC = 0.88, PPV = 0.88, SEN = 0.89	Tumor growth model + tumor shape prior + EM	DSC = 0.88, PPV = 0.92, SEN = 0.84
Havaei et al. [27]	BRATS 2013	INPUTCASCADECNN	Dice = 0.88, SPE = 0.89, SEN = 0.87	RF	Dice = 0.87, SPE = 0.85, SEN = 0.89
Kamnitsas et al. [29]	BRATS 2015	Multiscale 3D CNN + CRF	DSC = 0.849, PREC = 0.853, SEN = 0.877	—	—
Yi et al. [32]	BRATS 2015	3D fully CNN	ACC = 0.89	GLISTR algorithm	ACC = 0.88
Casamitjana et al. [33]	BRATS 2015	Three different 3D fully connected CNNs	ACC = 0.9969/0.9971/0.9971	—	—
Zhao et al. [36]	BRATS 2013	3D fully CNN + CRF	Dice = 0.87, PPV = 0.92, SEN = 0.83	CNN	Dice = 0.88, PPV = 0.88, SEN = 0.89
Alex et al. [38]	BRATS 2013/2015	SDAE	ACC = 0.85 ± 0.04/0.73 ± 0.25	—	—
Ibragimov et al. [39]	CT, MR and PET images	CNN	Dice = 0.818	—	—

Notes. BRATS = multimodal brain tumor segmentation dataset, including four MRI sequences (T1W, T1-postcontrast (T1c), T2W, and FLAIR); CNN = convolutional neural networks; HGG = high-grade gliomas; ACC = accuracy; RF = random forests; DNN = deep neural network; Average = the average values of sensitivity, specificity, and precision; LGG = low-grade gliomas; PPV = positive predictive value; SEN = sensitivity; DSC = dice similarity coefficient; INPUTCASCADECNN = cascaded architecture using input concatenation; EM = expectation maximization algorithm; SPE = specificity; PREC = precision; GLISRT (glioma image segmentation and registration); CRF = conditional random fields; SDAE = stacked denoising autoencoder.

manifold learning due to the limited training samples, DNN still demonstrated great potential for the clinical applications.

Various 2D CNN and 3D CNN models were proposed for brain tumor segmentation and were evaluated on public databases such as brain tumor segmentation (BRATS) challenges [18]. The data from BRATS consists of four MRI sequences, including T1W, T1-postcontrast (T1c), T2W, and FLAIR.

2D CNNs were firstly applied for 3D brain tumor segmentation with consideration of less modification to the existing models and less computational load. Zikic et al. [19] used a standard CNN architecture with two convolutional layers:

one followed by a max-pooling layer and the other followed by a fully connected layer and a softmax layer. Standard intensity preprocessing was used to remove scanner difference but without any postprocessing for the CNN output. They tested the proposed method on 20 high-grade cases from the training set of the BRATS 2013 challenge and obtained promising preliminary results. Actually, the 2D CNNs may not be sufficiently powerful for 3D segmentation; thus the information extracted axially, sagittally, and coronally should be combined. Lyksborg et al. [20] proposed a method based on an ensemble of 2D CNNs to fuse the segmentation from three orthogonal planes. The GrowCut algorithm [21] was

TABLE 2: Comparison of the performance of deep learning-based classification methods.

Publication	Type of images	Proposed methods		Comparison baseline	
		Method	Results	Method	Results
Reda et al. [40]	DW-MRI	SNCAE	ACC = 1, SEN = 1, SPE = 1	K^*	ACC = 0.943, SEN = 0.943, SPE = 0.944
Reda et al. [41]	DW-MRI	SNCAE	ACC = 1, SEN = 1, SPE = 1, AUC \approx 1	K^*	ACC = 0.943, SEN = 0.962, SPE = 0.926, AUC = 0.93
Zhu et al. [42]	T2-weighted, DWI and ADC	SAE	SBE = 0.8990 ± 0.0423 , SEN = 0.9151 ± 0.0253 , SPE = 0.8847 ± 0.0389	HOG features	SBE = 0.8814 ± 0.0534 , SEN = 0.9191 ± 0.0296 , SPE = 0.8696 ± 0.0563
Akkus et al. [43]	T1-postcontrast (T1C) and T2	Multiscale CNN	ACC = 0.877, SEN = 0.933, SPE = 0.822	—	—
Pan et al. [44]	BRATS 2014	CNN	SEN = 0.6667, SPE = 0.6667	NN	SEN = 0.5677, SPE = 0.5677
Hirata et al. [45]	FDG PET	CNN	ACC = 0.88	SUV _{max}	ACC = 0.80
Hirata et al. [46]	MET PET	CNN	ACC = 0.888 ± 0.055	SUV _{max}	ACC = 0.66
Teramoto et al. [47]	PET/CT	CNN	SEN = 0.901, with 4.9 FPs/case	Active contour filter	SEN = 0.901, with 9.8 FPs/case
Wang et al. [48]	FDG PET	CNN	ACC = 0.8564 ± 0.0809 , SEN = 0.8353 ± 0.1385 , SPE = 0.8775 ± 0.1030 , AUC = 0.9086 ± 0.0865	AdaBoost + D13	ACC = 0.8505 ± 0.0897 , SEN = 0.8565 ± 0.1346 , SPE = 0.8445 ± 0.1261 , AUC = 0.9143 ± 0.0751
Antropova et al. [51]	DCE-MRI	CNN ConvNet	AUC = 0.85	—	—

Notes. DW-MRI = diffusion-weighted magnetic resonance images; SNCAE = stacked nonnegativity-constrained autoencoders; ACC = accuracy; SEN = sensitivity; SPE = specificity; AUC = area under the receiver operating characteristic curve; K^* = K -Star, a classifier implemented in Weka toolbox [59]; DWI = diffusion-weighted imaging; ADC = apparent diffusion coefficient; SAE = stacked autoencoder; SBE = section-based evaluation; HOG = histogram of oriented gradient; CNN = convolutional neural network; BRATS = multimodal brain tumor segmentation dataset, including four MRI sequences (T1W, T1-postcontrast, T2W, and FLAIR); NN = neural network; FDG = fluorodeoxyglucose; PET = positron emission tomography; SUV_{max} = maximum standardized uptake value; MET = ¹¹C-methionine; CT = computed tomography; FP = false positive; AdaBoost = adaptive boosting; D13 = 13 diagnostic features.

TABLE 3: Comparison of the performance of deep learning-based survival prediction methods.

Publication	Type of images	Proposed methods		Comparison baseline	
		Method	Results	Method	Results
Liu et al. [52]	MRI	CNN + RF	ACC = 0.9545	CHF	ACC = 0.9091
Paul et al. [54]	Contrast-enhanced CT	CNN + SUFRA + RF	AUC = 0.935	TQF + DT	AUC = 0.712

Notes. MRI = magnetic resonance imaging; CNN = convolutional neural network; RF = random forest; ACC = accuracy; CHF = conventional histogram feature; CT = computer tomography; SUFRA = symmetric uncertainty feature ranking algorithm [60]; AUC = area under the receiver operating characteristic curve; TQF = traditional quantitative features; DT = decision tree.

also applied to smooth the segmentation of the complete tumor for postprocessing. They achieved better performance than axially trained 2D network and the ensemble method without GrowCut on BRATS 2014. It is worth noting that the combination of information from different orthogonal planes and the application of postprocessing algorithm contributed to this enhancement.

Instead of applying a known postprocessing algorithm such as Markov Random Fields (MRF) [22] for smoother segmentation, useful information provided by the neighboring voxels can also be integrated through the local structure prediction by taking the local dependencies of labels into consideration. Dvořák and Menze [23] proposed a method

combining local structure prediction and CNN, where K -means was used for generation of the label patch dictionary and then CNN was used for input prediction. Both labels of the neighboring pixels and the center pixels were taken into account in this method. They obtained state-of-the-art results on the BRATS 2014 dataset for brain tumor segmentation.

The main challenges of CNN lie in overfitting caused by the large amount of parameters and time-consuming training process. Some studies have applied appropriate training strategies to solve these problems. Pereira et al. [24, 25] used a deep CNN for the segmentation of gliomas in multisequence MRI and applied Dropout [26], leaky rectifier linear units, and small convolutional kernels to address

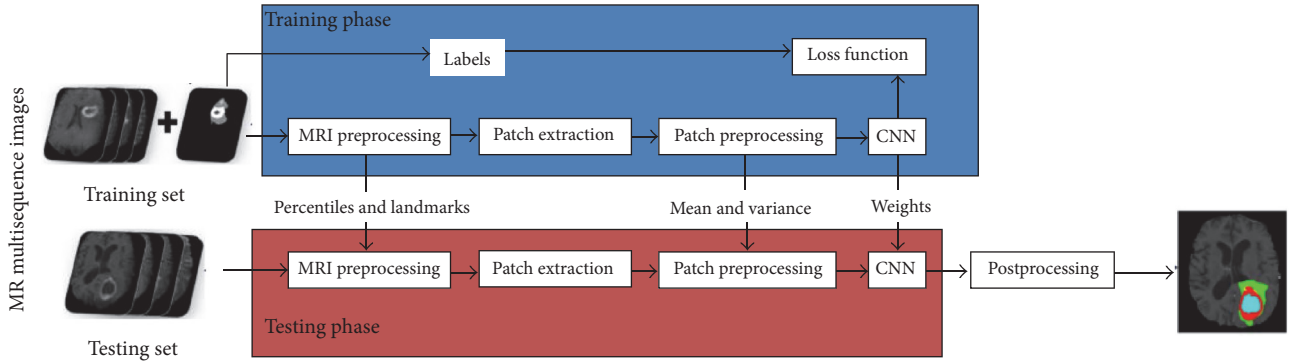


FIGURE 1: Framework of the proposed method. Image courtesy of Sérgio Pereira, Adriano Pinto, Victor Alves, and Carlos A. Silva, University of Minho.

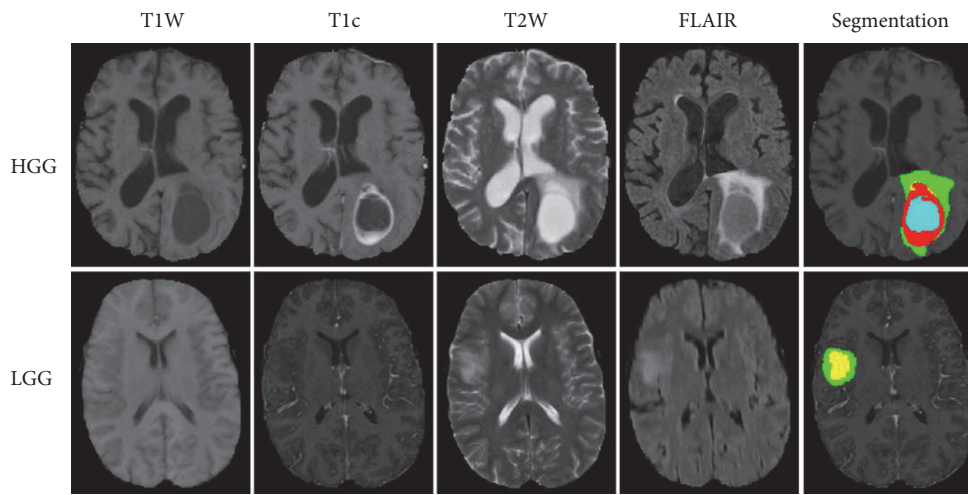


FIGURE 2: Example of brain tumor segmented into different tumor classes (green, edema; blue, necrosis; yellow, nonenhancing tumor; red, enhancing tumor) by the proposed method. Image courtesy of Sérgio Pereira, Adriano Pinto, Victor Alves, and Carlos A. Silva, University of Minho.

overfitting (Figure 1). They used different CNN architectures for low-grade glioma (LGG) and high-grade glioma (HGG). The convolutional layers were halved in the architecture for LGG. Data augmentation was employed in this study and was found useful. The examples of segmentation were shown in Figure 2. They obtained the first place on a 2013 public challenge dataset, and the second place in an on-site 2015 challenge. Proper structure improvement can accelerate the training process. Havaei et al. [27] proposed a variety of CNN models based on two-pathway and cascaded architectures, respectively, for tackling brain tumor segmentation, incorporating both local features and more global contextual features simultaneously. Their CNN allowed a 40-fold speed up using a convolutional implementation of a fully connected layer as a final layer. In addition, a 2-phase training procedure can solve the problem due to the imbalance of tumor labels. Compared to the currently published state-of-the-art methods, the results that Havaei et al. [27] reported on the 2013 BRATS test dataset was over 30 times faster. In addition, the cascaded method made refinement for the probability maps generated

by the base model, which made them one of the top 4 teams in BRATS 2015 [28].

To make full use of 3D information, 3D CNNs have been also developed in the recent two years for better segmentation performance. With consideration of the limitations in the existing models, a 3D CNN with a dual pathway and 11 layers was devised by Kamnitsas et al. [29]. The computational load of processing multimodal 3D data was also reduced by an efficient training scheme with dense training [30]. Due to conditional random fields (CRF) with the strong regularization ability for improving the segmentation, a 3D fully connected CRF [31] was incorporated with the proposed multiscale 3D CNN to remove false positive effectively. The proposed model was employed on BRATS 2015 for generalization testing and achieved top ranking performance.

Limited sample size is a key factor affecting the CNN performance. Yi et al. [32] proposed a 3D fully CNN with a modified nontrained convolutional layer that was able to achieve the enlargement of the training data size by incorporating information at pixel level instead of patient

level. The proposed method was evaluated on BRATS 2013 and BRATS 2015 and achieved superior performance.

Casamitjana et al. [33] tested three different 3D fully connected CNNs on the training datasets of BRATS 2015. The three models were based on the VGG architecture [34], learning deconvolution network [35], and a modification of multiscale 3D CNN [29] presented above, respectively. All these models obtained promising preliminary results, with an accuracy of 99.69%, 99.71%, and 99.71%, respectively.

Zhao et al. [36] proposed a method based on the integration of fully CNN and CRF [37]. In addition, this slice-by-slice tumor segmentation method enabled the acceleration of the segmentation process. The proposed method finally achieved comparative performance with the combination of FLAIR, T1c, and T2 images from BRATS 2013 and BRATS 2016 than those results on the combination of FLAIR, T1c, T1, and T2 images, which suggested that the proposed method was powerful and promising.

The requirement of large training database with manual labels constrains the application of CNN-based models, since manual annotations are usually unavailable or intractable in a large dataset. Therefore, semisupervised or weakly supervised learning should be considered as a substitute to supervised learning. Autoencoder-based models have shown advantage in model training with unlabeled data. Alex et al. [38] proposed a method based on weakly supervised stacked denoising autoencoders to segment brain lesion as well as reduce false positive. Due to the LGG samples in a limited size, transfer learning was employed in this study. LGG segmentation was achieved using a network pretrained by large HGG data and fine-tuned by limited data from 20 LGG patients. The proposed method achieved competitive performance on unseen BRATS 2013 and BRATS 2015 test data.

Besides lesion detection, accurate segmentation is also essential to radiotherapy planning. For head and neck cancer, Ibragimov et al. [39] proposed a classification scheme for automated segmentation of organs-at-risk (OARs) and tongue muscles based on deep learning and multimodal medical images including CT, MR, and PET. The promising results presented in this comprehensive study suggested that deep learning has great potential in radiotherapy treatment planning.

Regarding tumor segmentation, deep learning models can learn more abstract information or high-level feature representation from images and thus achieve better performance than those methods based on shallow structures. In addition, the combination of deep and shallow structures is more powerful than the single deep learning model. However, the challenges of deep learning models mainly lie in how to avoid overfitting and to accelerate the training process. Specific techniques such as Dropout, Leaky Rectifier Linear Units, and small convolutional kernels have been developed to address overfitting, and proper improvements of deep learning architectures have been made to accelerate the training. It is worth noting that the dataset used in these studies were multimodal; thus the information provided by the molecular imaging and anatomical imaging can be integrated effectively. The integrated information may be utilized efficiently by deep

learning models and thus contribute to better segmentation performance.

Since 2013, the dataset of BRATS benchmark was divided into five classes according to the pathological features presented in different modalities. Each class has a specific manual label, including healthy, necrosis, edema, and nonenhancing and enhanced tumor. In addition, three tumor regions were defined as the gold standard of segmentation, including complete tumor region (necrosis, edema, and nonenhancing and enhanced tumor), core tumor region (necrosis and nonenhancing and enhanced tumor), and enhancing tumor region (enhanced tumor). Generally, deep learning models achieved best performance in HGG segmentation. The relatively poor performance in LGG segmentation may be caused by sample imbalance, since less LGG patients were included in the BRATS benchmark. Besides, the inherent class imbalance of the dataset was also likely to lead to the poor performance in enhancing tumor region segmentation. For example, the real proportion of five classes in BRATS 2015 is 92.42%, 0.43%, 4.87%, 1.02%, and 1.27% for healthy, necrosis, edema, and nonenhancing and enhancing tumor, respectively [29].

3. Deep Learning in Cancer Classification

For early detection of prostate cancer, deep learning techniques such as CNN and stacked autoencoders (SAE) have been applied on diffusion-weighted magnetic resonance images (DW-MRI) and multiparametric MRI. Reda et al. [40] used the cumulative distribution function (CDF) of refined apparent diffusion coefficient (ADC) for the prostate tissues at different b -values as global features and trained a deep autoencoder network with stacked nonnegativity-constrained autoencoders (SNCAE) for classification of benign and malignant prostate tumors. Reda et al. [41] also proposed an automated noninvasive CAD system based on DW-MRI and SNCAE for diagnosing prostate cancer. There were three steps for the proposed scheme: (i) localizing and segmenting prostate with a deformable nonnegative matrix factorization- (NMF-) based model; (ii) constructing the CDF of estimated ADC as extracted discriminatory characteristics; (iii) classifying benign and malignant prostates with SNCAE classifier (Figure 3). The SNCAE-based method proposed by Reda et al. [41] has achieved excellent classification performance on the DW-MRI data from 53 subjects, but this method still needs several preprocessing steps leveraging hand-crafted features, which may greatly affect the computational load of the classification. Zhu et al. [42] proposed a method based on SAE and multiple random forest classifiers for prostate cancer detection, in which a SAE-based model was employed to extract latent high-level feature representation from multiparametric MR images for the first step; then multiple random forest classifiers were implemented for refinement of prostate cancer detection results. Though the proposed method has been proved effective on 21 prostate cancer patients, it should still be further validated on a large sample.

CNN has been widely used in brain tumor evaluation, grading, and detection. The codeletion of chromosome arms

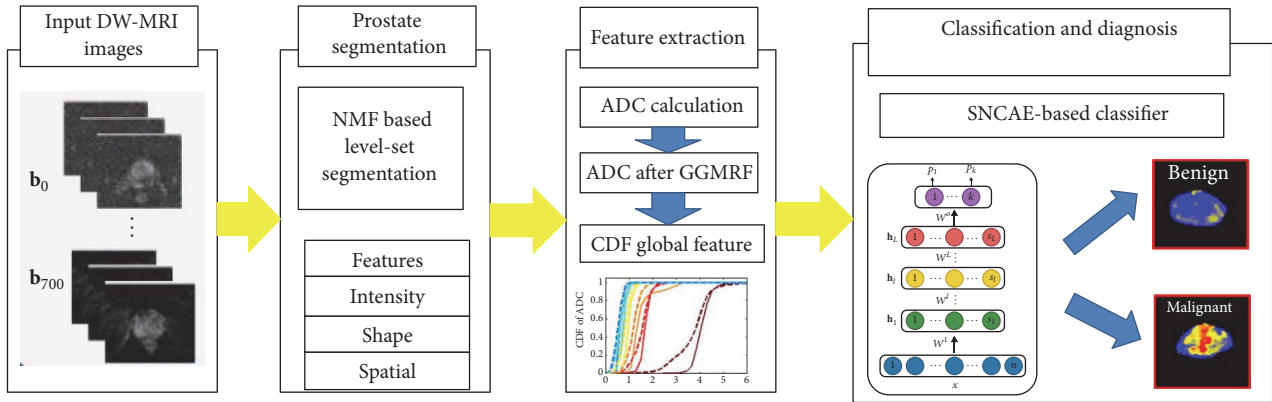


FIGURE 3: Framework of the DW-MRI CAD system for prostate cancer classification. Image courtesy of Islam Reda et al.

1p/19q status prediction is clinically important for it plays an important role in treatment planning of LGG. To find out a potential noninvasive alternative to surgical biopsy and histopathological analysis, Akkus et al. [43] applied multiscale CNN to predict 1p/19q status for effective treatment planning of LGG based on T1c and T2W images. The results suggested that artificial data augmentation potentially enhance the performance by improving generalization ability of the multiscale CNN and avoiding overfitting. Pan et al. [44] compared the performance of Neural Networks (NN) and CNN for brain tumor grading. They found that CNN outperformed NN for grading, but the more complex structure of CNN did not show better results in the experiment. Because different treatment strategies are needed for glioblastoma and primary central nervous system lymphoma, it is clinically important to differentiate them from each other. Hirata et al. [45] applied CNN for differentiation of brain FDG PET between glioblastoma and primary central nervous system lymphoma (PCNSL). The method supplemented by the manual-drawing ROIs achieved higher overall accuracy on both slice-based and patient-based analysis than that without ROI masking, which suggested that CNN may be more powerful combined with an appropriate tumor segmentation technique. To achieve fully automated quantitative analysis of the brain tumor metabolism based on ^{11}C -methionine (MET) PET, Hirata et al. [46] applied CNN to extract the tumor slices from the whole brain images based on MET PET and achieved better classification performance than maximum standardized uptake value (SUV_{\max}) based method. With high specificity, the CNN technique has been proven to be effective in detecting the slices with tumor lesions on MET PET from 45 glioma patients as a slice classifier.

CNN has been applied in computer-aided detection of lung tumors. Teramoto et al. [47] proposed an ensemble false positive- (FP-) reduction method based on conventional shape/metabolic features and CNN technique. The proposed method removed approximately half of the FPs in the previous methods. Wang et al. [48] compared CNN and four classical machine learning methods (random forests, support vector machines, adaptive boosting, and artificial

neural network) for the classification of mediastinal lymph node metastasis of non-small-cell lung cancer (NSCLC) from ^{18}F -FDG PET/CT images. In this study, it was reported that CNN was not significantly different from the best traditional methods or human doctors for classifying mediastinal lymph node metastasis of NSCLC from PET/CT images.

The training data of a small size is considered as the main reason for the limited performance of deep learning. Khan and Yong [49] reported that the hand-crafted features outperformed the deep learned features in medical image modality classification with small datasets. Cho et al. [50] presented a study on determining how much training dataset is necessary to achieve high classification accuracy. With CNN, the accuracy of different body part (like brain, neck, shoulder, etc.) classification based on CT images was greatly improved as the training sample size increased from 5 to 200. CNN with deeper architecture might outperform other approaches by increasing the training data and applying the training strategy of transfer learning and fine-tuning [13]. Transfer learning has been used in medical imaging applications, as a key strategy to solving the problem of insufficient training data. Antropova et al. [51] used the CNN architecture ConvNet pretrained by AlexNet on the ImageNet database for breast cancer classification on dynamic contrast-enhanced MR images (DCE-MRI) and showed that transfer learning can enhance the predicting performance of breast cancer malignancy. Transfer learning is commonly used in CNN-based models for network initialization when the training data is limited and the fine-tuning of the parameters is usually required for the specific tasks. However, the theoretical understanding on why transfer learning accelerates the learning process and improves the generalization ability remains unknown.

Deep learning has been applied for the classification of prostate cancer, brain tumor, lung tumor, and breast cancer based on molecular imaging. Most studies mentioned above have proven the better performance of deep learning, but a few studies indicated that the results achieved by deep learning models were not significantly better than the best conventional methods. The various results suggested that deep learning models with well-designed architecture have

great potential to achieve excellent classification performance. Besides, deep learning models may achieve better performance combined with shallow structures for contextual information integration. Sufficient training data is required to prevent overfitting and to improve generalization ability, which is still a challenge in many applications. In practice, data augmentation, pretraining, and fine-tuning were often applied to tackle these problems.

4. Deep Learning in Survival Prediction

Besides tumor segmentation and classification, deep learning has also been employed in predicting patients' survival. Liu et al. [52] applied the CNN-F architecture [53] pretrained on ILSVRC-2012 with the ImageNet dataset for predicting survival time based on brain MR images, achieving the highest accuracy of 95.45%. Paul et al. [54] predicted short- and long-term survivors of non-small-cell adenocarcinoma lung cancer on contrast CT images, with 5 postrectified linear unit features extracted from a VGG-F pretrained CNN and 5 traditional features. They obtained an accuracy of 90% and AUC of 0.935. With high accuracy, pretrained CNN architectures may have potential to predict survival of cancer patients in the future.

5. Trends and Challenges

Along with the promising performance achieved by deep learning in molecular imaging of cancer, challenges and inherent trends have been posed in the following aspects.

Firstly, although deep learning has outperformed other methods based on shallow structures and achieved promising results, the underlying theory needs to be further investigated. The numbers of layers and nodes in each layer are usually determined by experience, and the learning rate and the regularization strength are chosen subjectively. Two key components should be considered for devising the deep learning model: the architecture and the depth. For model configuration, different architectures should be evaluated for the specific task.

Secondly, the insufficient data is a common challenging when employing deep learning techniques in many applications. In this case, effective training schemes should be exploited to cope with this problem. The strategies of data augmentation, pretraining, and fine-tuning have been applied in some studies, but the underlying mechanism of some of these strategies still remains unclear. It is suggested that public database of molecular imaging should be established. In addition, integrating information from multimodal imaging may improve the model performance. Moreover, it is worth noting that the sample imbalance should be avoided during training process by keeping the balance of sample size between the subtypes of a specific cancer.

Thirdly, as manual annotations are difficult or expensive in a large dataset, semisupervised and unsupervised learning are highly required in the future development [4]. Unsupervised learning and the generation of features layer by layer has made the deep architecture training possible and has improved the signal-to-noise ratio at lower levels

compared to supervised learning algorithm [55–57], while semisupervised methods may achieve a good generalization capability and superior performance compared to unsupervised learning [14].

Finally, given that the abstract information extracted by deep learning models is not well understood, the correlation between the high-level feature and clinical characteristics in molecular imaging should be established to increase the reliability of deep learning techniques. Typically, these clinical characteristics of molecular imaging include the expression and activity of specific molecules (e.g., proteases and protein kinases) and biological processes (e.g., apoptosis, angiogenesis, and metastasis) [58]. Ideally, the relationship between the features output in each layer and the clinical characteristics acquired by surgical biopsy and pathological analysis is expected to be validated. In that case, the layers without significant correlation with clinical characteristics can be removed, which may increase the effectiveness of the proposed model and reduces computational resources.

6. Conclusion

We present a comprehensive review of diverse applications of deep learning in molecular imaging of cancer. The applications of deep learning in cancer mainly included tumor lesion segmentation, cancer classification, and survival prediction. CNN-based models are most commonly used in these studies and have achieved promising results. Despite the encouraging performance, studies are still required for further investigations about model optimization, public database establishment, and unsupervised learning as well as of the correlation between high-level features and clinical characteristics of cancer. In order to solve these problems, clinicians and engineers should work together by taking complementary expertise and advantages. In conclusion, deep learning as a promising and powerful tool will aid and improve the application of molecular imaging in cancer diagnosis and treatment.

Conflicts of Interest

The authors declare that there are no conflicts of interest regarding the publication of this paper.

Authors' Contributions

Yong Xue and Shihui Chen contributed equally to this work and they are co-first authors.

Acknowledgments

The study was jointly funded by Guangdong Scientific Research Funding in Medicine (no. B2016031), Shenzhen High-Caliber Personnel Research Funding (no. 000048), Special Funding Scheme for Supporting the Innovation and Research of Shenzhen High-Caliber Overseas Intelligence (KQCX2014051910324353), and Shenzhen Municipal Scheme for Basic Research (no. JCYJ20160307114900292).

References

- [1] R. L. Siegel, K. D. Miller, and A. Jemal, "Cancer statistics, 2016," *CA: A Cancer Journal for Clinicians*, vol. 66, no. 1, pp. 7–30, 2016.
- [2] R. Etzioni, N. Urban, S. Ramsey et al., "The case for early detection," *Nature Reviews Cancer*, vol. 3, no. 4, pp. 243–252, 2003.
- [3] D. A. Mankoff, "A definition of molecular imaging," *Journal of Nuclear Medicine*, vol. 48, no. 6, pp. 18N–21N, 2007.
- [4] Y. LeCun, Y. Bengio, and G. Hinton, "Deep learning," *Nature*, vol. 521, no. 7553, pp. 436–444, 2015.
- [5] L. Deng, "A tutorial survey of architectures, algorithms, and applications for deep learning," *APSIPA Transactions on Signal and Information Processing*, vol. 3, 2014.
- [6] J. Schmidhuber, "Deep learning in neural networks: an overview," *Neural Networks*, vol. 61, pp. 85–117, 2015.
- [7] J.-Z. Cheng, D. Ni, Y.-H. Chou et al., "Computer-Aided Diagnosis with Deep Learning Architecture: Applications to Breast Lesions in US Images and Pulmonary Nodules in CT Scans," *Scientific Reports*, vol. 6, Article ID 24454, 2016.
- [8] A. Işin, C. Direkçöğlü, and M. Şah, "Review of MRI-based Brain Tumor Image Segmentation Using Deep Learning Methods," in *Proceedings of the 12th International Conference on Application of Fuzzy Systems and Soft Computing, ICAFS 2016*, pp. 317–324, aut, August 2016.
- [9] Y. Guo, Y. Liu, A. Oerlemans, S. Lao, S. Wu, and M. S. Lew, "Deep learning for visual understanding: a review," *Neurocomputing*, vol. 187, pp. 27–48, 2016.
- [10] H. Greenspan, B. Van Ginneken, and R. M. Summers, "Guest Editorial Deep Learning in Medical Imaging: Overview and Future Promise of an Exciting New Technique," *IEEE Transactions on Medical Imaging*, vol. 35, no. 5, pp. 1153–1159, 2016.
- [11] C. Szegedy, W. Liu, Y. Jia et al., "Going deeper with convolutions," in *Proceedings of the IEEE Conference on Computer Vision and Pattern Recognition (CVPR '15)*, pp. 1–9, Boston, Mass, USA, June 2015.
- [12] M. Oquab, L. Bottou, I. Laptev, and J. Sivic, "Is object localization for free? - Weakly-supervised learning with convolutional neural networks," in *Proceedings of the IEEE Conference on Computer Vision and Pattern Recognition, CVPR 2015*, pp. 685–694, June 2015.
- [13] Y. Bengio, A. Courville, and P. Vincent, "Representation learning: a review and new perspectives," *IEEE Transactions on Pattern Analysis and Machine Intelligence*, vol. 35, no. 8, pp. 1798–1828, 2013.
- [14] D. Zhou, L. Tran, J. Wang, and J. Li, "A comparative study of two prediction models for brain tumor progression," in *Proceedings of the IS&T/SPIE Electronic Imaging*, vol. 9399, pp. 93990W–93997, San Francisco, Calif, USA.
- [15] L. Tran, D. Banerjee, J. Wang et al., "High-dimensional MRI data analysis using a large-scale manifold learning approach," *Machine Vision and Applications*, vol. 24, no. 5, pp. 995–1014, 2013.
- [16] S. T. Roweis and L. K. Saul, "Nonlinear dimensionality reduction by locally linear embedding," *Science*, vol. 290, no. 5500, pp. 2323–2326, 2000.
- [17] D. L. Donoho and C. Grimes, "Hessian eigenmaps: locally linear embedding techniques for high-dimensional data," *Proceedings of the National Academy of Sciences of the United States of America*, vol. 100, no. 10, pp. 5591–5596, 2003.
- [18] H. B. Menze, A. Jakab, S. Bauer et al., "The multimodal brain tumor image segmentation benchmark (BRATS)," *IEEE Transactions on Medical Imaging*, vol. 34, no. 10, pp. 1993–2024, 2015.
- [19] D. Zikic, Y. Ioannou, M. Brown et al., "Segmentation of brain tumor tissues with convolutional neural networks," *Proceedings MICCAI-BRATS*, pp. 36–39, 2014.
- [20] M. Lyksborg, O. Puonti, M. Agn, and R. Larsen, "An Ensemble of 2D Convolutional Neural Networks for Tumor Segmentation," in *Image Analysis*, R. R. Paulsen and K. S. Pedersen, Eds., vol. 9127 of *Lecture Notes in Computer Science*, pp. 201–211, Springer International Publishing, Cham, Switzerland, 2015.
- [21] V. Vezhnevets and V. Konouchine, "GrowCut- Interactive multi-label N-D image segmentation by cellular automata," in *Proceedings of the 15th International Conference on Computer Graphics and Vision, GraphiCon 2005*, June 2005.
- [22] B. H. Menze, K. Van Leemput, D. Lashkari, M.-A. Weber, N. Ayache, and P. Golland, "A generative model for brain tumor segmentation in multi-modal images," in *Proceedings of the International Conference on Medical Image Computing and Computer-Assisted Intervention*, vol. 13, pp. 151–159, 2010.
- [23] P. Dvořák and B. Menze, "Local Structure Prediction with Convolutional Neural Networks for Multimodal Brain Tumor Segmentation," in *Medical Computer Vision: Algorithms for Big Data*, vol. 9601 of *Lecture Notes in Computer Science*, pp. 59–71, Springer International Publishing, Cham, Switzerland, 2016.
- [24] S. Pereira, A. Pinto, V. Alves, and C. A. Silva, "Deep Convolutional Neural Networks for the Segmentation of Gliomas in Multi-sequence MRI," in *Brainlesion: Glioma, Multiple Sclerosis, Stroke and Traumatic Brain Injuries*, vol. 9556 of *Lecture Notes in Computer Science*, pp. 131–143, Springer International Publishing, Cham, Switzerland, 2016.
- [25] S. Pereira, A. Pinto, V. Alves, and C. A. Silva, "Brain Tumor Segmentation Using Convolutional Neural Networks in MRI Images," *IEEE Transactions on Medical Imaging*, vol. 35, no. 5, pp. 1240–1251, 2016.
- [26] N. Srivastava, G. Hinton, A. Krizhevsky, I. Sutskever, and R. Salakhutdinov, "Dropout: a simple way to prevent neural networks from overfitting," *The Journal of Machine Learning Research*, vol. 15, no. 1, pp. 1929–1958, 2014.
- [27] M. Havaei, A. Davy, D. Warde-Farley et al., "Brain tumor segmentation with Deep Neural Networks," *Medical Image Analysis*, vol. 35, pp. 18–31, 2017.
- [28] M. Havaei, F. Dutil, C. Pal, H. Larochelle, and P. Jodoin, "A Convolutional Neural Network Approach to Brain Tumor Segmentation," in *Brainlesion: Glioma, Multiple Sclerosis, Stroke and Traumatic Brain Injuries*, vol. 9556 of *Lecture Notes in Computer Science*, pp. 195–208, Springer International Publishing, Cham, Switzerland, 2016.
- [29] K. Kamnitsas, C. Ledig, V. F. J. Newcombe et al., "Efficient multi-scale 3D CNN with fully connected CRF for accurate brain lesion segmentation," *Medical Image Analysis*, vol. 36, pp. 61–78, 2017.
- [30] J. Long, E. Shelhamer, and T. Darrell, "Fully convolutional networks for semantic segmentation," in *Proceedings of the IEEE Conference on Computer Vision and Pattern Recognition (CVPR '15)*, pp. 3431–3440, IEEE, Boston, Mass, USA, June 2015.
- [31] P. Kr Henb HL and V. Koltun, "Efficient inference in fully connected crfs with gaussian edge potentials," in *Proceedings of the Advances in neural information processing systems*, pp. 109–117, 2011.

- [32] D. Yi, M. Zhou, Z. Chen et al., “3-D Convolutional Neural Networks for Glioblastoma Segmentation,” 2016, <https://arxiv.org/abs/1611.04534>.
- [33] A. Casamitjana, S. Puch, A. Aduriz et al., “3d convolutional networks for brain tumor segmentation,” in *Proceedings of the MIC-CAI Challenge on Multimodal Brain Tumor Image Segmentation (BRATS)*, pp. 65–68, 2016.
- [34] K. Simonyan and A. Zisserman, “Very deep convolutional networks for large-scale image recognition,” 2014, <https://arxiv.org/abs/1409.1556>.
- [35] H. Noh, S. Hong, and B. Han, “Learning deconvolution network for semantic segmentation,” in *Proceedings of the 15th IEEE International Conference on Computer Vision, ICCV 2015*, pp. 1520–1528, ch1, December 2015.
- [36] X. Zhao, Y. Wu, G. Song et al., “A deep learning model integrating FCNNs and CRFs for brain tumor segmentation,” 2017, <https://arxiv.org/abs/1702.04528>.
- [37] S. Zheng, S. Jayasumana, B. Romera-Paredes et al., “Conditional random fields as recurrent neural networks,” in *Proceedings of the 15th IEEE International Conference on Computer Vision, ICCV 2015*, pp. 1529–1537, ch1, December 2015.
- [38] V. Alex, K. Vaidhya, S. Thirunavukkarasu et al., “Semi-supervised Learning using Denoising Autoencoders for Brain Lesion Detection and Segmentation,” 2016, <https://arxiv.org/abs/1611.08664>.
- [39] B. Ibragimov, F. Pernus, P. Strojjan, and L. Xing, “TH-CD-206-05: Machine-Learning Based Segmentation of Organs at Risks for Head and Neck Radiotherapy Planning,” *Medical Physics*, vol. 43, no. 6, pp. 3883–3883, 2016.
- [40] I. Reda, A. Shalaby, F. Khalifa et al., “Computer-aided diagnostic tool for early detection of prostate cancer,” in *Proceedings of the 23rd IEEE International Conference on Image Processing, ICIP 2016*, pp. 2668–2672, usa, September 2016.
- [41] I. Reda, A. Shalaby, M. Elmogy et al., “A comprehensive non-invasive framework for diagnosing prostate cancer,” *Computers in Biology and Medicine*, vol. 81, pp. 148–158, 2017.
- [42] Y. Zhu, L. Wang, M. Liu et al., “MRI-based prostate cancer detection with high-level representation and hierarchical classification,” *Medical physics*, vol. 44, no. 3, pp. 1028–1039, 2017.
- [43] Z. Akkus, I. Ali, J. Sedlar et al., “Predicting 1p19q Chromosomal Deletion of Low-Grade Gliomas from MR Images using Deep Learning,” 2016, <https://arxiv.org/abs/1611.06939>.
- [44] Y. Pan, W. Huang, Z. Lin et al., “Brain tumor grading based on Neural Networks and Convolutional Neural Networks,” in *Proceedings of the 37th Annual International Conference of the IEEE Engineering in Medicine and Biology Society, EMBC 2015*, pp. 699–702, August 2015.
- [45] K. Hirata, W. Takeuchi, S. Yamaguchi et al., “Convolutional neural network can help differentiate FDG PET images of brain tumor between glioblastoma and primary central nervous system lymphoma,” *The Journal of Nuclear Medicine*, vol. 57, 2, 1855.
- [46] K. Hirata, W. Takeuchi, S. Yamaguchi et al., “Use of convolutional neural network as the first step of fully automated tumor detection on 11C-methionine brain PET,” *The Journal of Nuclear Medicine*, vol. 57, 2, p. 38, 2016.
- [47] A. Teramoto, H. Fujita, O. Yamamuro, and T. Tamaki, “Automated detection of pulmonary nodules in PET/CT images: Ensemble false-positive reduction using a convolutional neural network technique,” *Medical Physics*, vol. 43, no. 6, pp. 2821–2827, 2016.
- [48] H. Wang, Z. Zhou, Y. Li et al., “Comparison of machine learning methods for classifying mediastinal lymph node metastasis of non-small cell lung cancer from 18F-FDG PET/CT images,” *EJNMMI Research*, vol. 7, no. 1, article no. 11, 2017.
- [49] S. Khan and S.-P. Yong, “A comparison of deep learning and hand crafted features in medical image modality classification,” in *Proceedings of the 3rd International Conference on Computer and Information Sciences, ICCOINS 2016*, pp. 633–638, mys, August 2016.
- [50] J. Cho, K. Lee, E. Shin et al., “How much data is needed to train a medical image deep learning system to achieve necessary high accuracy: under review as a conference paper at ICLR 2016,” 2016.
- [51] N. Antropova, B. Huynh, and M. Giger, “SU-D-207B-06: Predicting Breast Cancer Malignancy On DCE-MRI Data Using Pre-Trained Convolutional Neural Networks,” *Medical Physics*, vol. 43, no. 6Part4, pp. 3349–3350, 2016.
- [52] R. Liu, L. O. Hall, D. B. Goldgof, M. Zhou, R. A. Gatenby, and K. B. Ahmed, “Exploring deep features from brain tumor magnetic resonance images via transfer learning,” in *Proceedings of the 2016 International Joint Conference on Neural Networks, IJCNN 2016*, pp. 235–242, can, July 2016.
- [53] K. Chatfield, K. Simonyan, A. Vedaldi, and A. Zisserman, “Return of the Devil in the Details: Delving Deep into Convolutional Nets,” in *Proceedings of the British Machine Vision Conference 2014*, pp. 6.1-6.12, Nottingham.
- [54] R. Paul, S. H. Hawkins, Y. Balagurunathan et al., “Deep Feature Transfer Learning in Combination with Traditional Features Predicts Survival Among Patients with Lung Adenocarcinoma,” *Tomography*, vol. 2, no. 4, pp. 388–395, 2016.
- [55] G. E. Hinton and R. R. Salakhutdinov, “Reducing the dimensionality of data with neural networks,” *American Association for the Advancement of Science. Science*, vol. 313, no. 5786, pp. 504–507, 2006.
- [56] Y. Bengio, “Learning deep architectures for AI,” *Foundations and Trends in Machine Learning*, vol. 2, no. 1, pp. 1–27, 2009.
- [57] D. Erhan, Y. Bengio, A. Courville, P.-A. Manzagol, P. Vincent, and S. Bengio, “Why does unsupervised pre-training help deep learning?” *Journal of Machine Learning Research*, vol. 11, pp. 625–660, 2010.
- [58] R. Weissleder, “Molecular imaging in cancer,” *Science*, vol. 312, no. 5777, pp. 1168–1171, 2006.
- [59] M. Hall, E. Frank, G. Holmes, B. Pfahringer, P. Reutemann, and I. H. Witten, “The WEKA data mining software: an update,” *ACM SIGKDD Explorations Newsletter*, vol. 11, no. 1, pp. 10–18, 2009.
- [60] L. Yu and H. Liu, “Feature selection for high-dimensional data: A fast correlation-based filter solution,” in *Proceedings of the 20th international conference on machine learning (ICML-03)*, pp. 856–863, 2003.

Research Article

Head and Neck Cancer Tumor Segmentation Using Support Vector Machine in Dynamic Contrast-Enhanced MRI

Wei Deng,^{1,2} Liangping Luo,³ Xiaoyi Lin,⁴ Tianqi Fang,⁴ Dexiang Liu,^{1,2}
Guo Dan,^{4,5} and Hanwei Chen^{1,2}

¹Department of Radiology, Guangzhou Panyu Central Hospital, Guangzhou, China

²Medical Imaging Institute of Panyu, Guangzhou, China

³Medical Imaging Center, The First Affiliated Hospital of Jinan University, Guangzhou, China

⁴National-Regional Key Technology Engineering Laboratory for Medical Ultrasound, Guangdong Key Laboratory for Biomedical Measurements and Ultrasound Imaging, School of Biomedical Engineering, Health Science Centre, Shenzhen University, Shenzhen, China

⁵Center for Neurorehabilitation, Shenzhen Institute of Neuroscience, Shenzhen 518057, China

Correspondence should be addressed to Guo Dan; danguo@szu.edu.cn and Hanwei Chen; docterwei@sina.com

Received 7 April 2017; Revised 18 July 2017; Accepted 6 August 2017; Published 7 September 2017

Academic Editor: Ziyue Xu

Copyright © 2017 Wei Deng et al. This is an open access article distributed under the Creative Commons Attribution License, which permits unrestricted use, distribution, and reproduction in any medium, provided the original work is properly cited.

Objective. We aimed to propose an automatic method based on Support Vector Machine (SVM) and Dynamic Contrast-Enhanced Magnetic Resonance Imaging (DCE-MRI) to segment the tumor lesions of head and neck cancer (HNC). **Materials and Methods.** 120 DCE-MRI samples were collected. Five curve features and two principal components of the normalized time-intensity curve (TIC) in 80 samples were calculated as the dataset in training three SVM classifiers. The other 40 samples were used as the testing dataset. The area overlap measure (AOM) and the corresponding ratio (CR) and percent match (PM) were calculated to evaluate the segmentation performance. The training and testing procedure was repeated for 10 times, and the average performance was calculated and compared with similar studies. **Results.** Our method has achieved higher accuracy compared to the previous results in literature in HNC segmentation. The average AOM with the testing dataset was 0.76 ± 0.08 , and the mean CR and PM were $79 \pm 9\%$ and $86 \pm 8\%$, respectively. **Conclusion.** With improved segmentation performance, our proposed method is of potential in clinical practice for HNC.

1. Introduction

Head and neck cancer (HNC) is an aggressive cancer at the head and neck region with high incidence in southern China especially in Hong Kong and Guangdong [1]. Medical imaging has been very important in the diagnosis and treatment of HNC. Dynamic contrast-enhanced magnetic resonance imaging (DCE-MRI) is an imaging method in which T1-weighted MRI scans are acquired dynamically after injection of MRI contrast agent, providing information about the characteristics of the physiological procedure. DCE-MRI tracks the diffusion of the contrast agent (a paramagnetic substance, normally Gadolinium-based) over time into the tissue by repeated imaging to reflect hemodynamic information such as the formation and permeability of microvascular

in living tumor [2]. The DCE-MRI image stores the time-intensity curve (TIC), which is different among tissues, like cancer, normal soft tissue, bone, and so on. Compared with the traditional MRI images and CT images, the differences in DCE-MRI images among tissues are more characteristic [3].

The diagnosis and treatment of HNC require accurate tumor lesion segmentation. Regarded as the ground truth, artificial segmentation operated by experienced radiologists is nonetheless time-consuming, and the accuracy is limited by the experience of radiologists. In recent years, automatic segmentation has attracted much attention. Machine learning algorithms have been applied in the segmentation of HNC, such as supervised learning, unsupervised learning, semisupervised learning, and enhanced learning. These

automatic segmentation methods may reduce the subjectivity and improve the quality in the segmentation tasks.

Among these methods, Support Vector Machine (SVM), a supervised learning algorithm, has showed great superiority with small sample size of data [4]. In this study we aimed to develop an automatic segmentation method for HNC based on DCE-MRI by using SVM.

2. Materials and Methods

2.1. DCE-MRI Data. In our study, all subjects were recruited from The First Affiliated Hospital, Sun Yat-sen University. DCE-MRI was performed on a 3.0-T system (Magnetom Trio, Siemens) with field of view (FOV) of $22 \times 22 \times 6$ cm (AP \times RL \times FH), a flip angle of 15° , and scanning time of 6 minute 47 seconds with 65 dynamic scans, 5.9 seconds per scan. The contrast agent gadodiamide Gd-DTPA (Omniscan; Nycomed, Oslo, Norway) was injected intravenously as a bolus into the blood at around the 8th dynamic acquisition using a power injector system (Spectris; Medrad, Indianola, Pennsylvania), immediately followed by a 25-mL saline flush at a rate of 3.5 mL per second. The dose of Gd-DTPA was 0.1 mmol/(kg body weight) for each patient. The reconstructed DCE-MRI images were a 4D matrix ($144 \times 144 \times 20 \times 65$) with 20 slices.

One hundred and twenty samples of DCE-MRI images containing the HNC tumor lesions were used as our database. Each sample was the DCE-MRI time series of a slice and thus was a $144 \times 144 \times 65$ matrix. Eighty samples were selected randomly as the training dataset while the remaining 40 samples were the testing dataset to verify the accuracy of segmentation.

2.2. Feature Extraction. Before extracting the features from the TIC in the DCE-MRI images, we performed the normalization as [8]

$$i_{\text{real}}(t) = \frac{i_n(t) - i(\text{pre})}{i(\text{pre})}, \quad (1)$$

where $i_{\text{real}}(t)$ denotes the final normalized TIC, $i_n(t)$ denotes the original TIC, and $i(\text{pre})$ denotes the average intensity in the first eight scans (before the injection of contrast agent) of $i_n(t)$.

In several studies some features had already been extracted from DCE-MRI images and successfully applied to classify the tumors from the surrounding tissue [8, 9]. In our study, with the normalized TIC ($i_{\text{real}}(t)$), the same TIC features were calculated. The maximum intensity was calculated as

$$i_{\text{max}} = \max(i_{\text{real}}(t)). \quad (2)$$

The time of reaching the maximum intensity, namely, time to peak, was calculated as

$$i_{\text{real}}(t_{\text{peak}}) = \max(i_{\text{real}}(t)). \quad (3)$$

The onset time was defined as the time to reach 10% of the maximum signal intensity after the 8th time point:

$$\begin{aligned} t_{\text{onset}} &= t_{10\%} - t_8, \\ i(t_{10\%}) &= i_{\text{max}} * 10\%. \end{aligned} \quad (4)$$

The wash-in rate was defined as the mean gradient between the two time points of t_{onset} and the maximum intensity:

$$\Delta_{\text{washin}} = \frac{(i_{\text{real}}(t_{\text{peak}}) - i_{\text{real}}(t_{\text{onset}}))}{(t_{\text{peak}} - t_{\text{onset}})}. \quad (5)$$

The wash-out rate was defined as the mean gradient between t_{peak} and the 65th time point:

$$\Delta_{\text{washout}} = \frac{(i_{\text{real}}(t_{\text{peak}}) - i_{\text{real}}(t_{65}))}{(t_{65} - t_{\text{peak}})}. \quad (6)$$

Besides, we also used Principal Component Analysis (PCA) [10] in this study to extract the principal components of the TIC. We chose the first two components (the eigenvector with the two highest eigenvalues) from PCA results and then multiplied them by the original data to produce two features. These two new features were used in the segmentation tasks.

2.3. SVM Training and Testing

2.3.1. SVM Training. For the training dataset of 80 samples, we firstly carefully drew some rectangular regions of interest (ROIs) for 4 regions, namely, the tumor lesions, the vessels, the normal tissue, and the cavity. This was done by an experienced radiologist (Dr. Wei Deng, 12 years' experience in Radiology) in ImageJ (National Institutes of Health, Bethesda, MD) and double-checked by another experienced radiologist with 14 years' experience who were blind to our study. We then calculated the mean TIC curve for the four regions, respectively, in the 80 samples as

$$i_{\text{aver}}(t, j) = \frac{\sum_{j=1}^k i(t, j)}{k}, \quad t = 1, \dots, 65, \quad (7)$$

where $i_{\text{aver}}(t, j)$ denotes the mean TIC in this ROI, $i(t, j)$ denotes the TIC of a voxel, and k denotes the total number of voxels. Thus, with 80 samples, we obtained 80×4 average TICs. We then calculated the 7 features (5 TIC characteristics, and 2 by PCA) for all the 320 TICs. We labeled these features with their corresponding type (tumor, vessel, normal tissue, and cavity). These features and labels formed our training dataset.

For SVM training, we used the MATLAB toolbox libsvm 3.17 (<http://www.csie.ntu.edu.tw/~cjlin/libsvm/>). After normalized across different samples, the training dataset was used to train three SVM classifiers. We tried and compared between the five curve features and the two PCA features and selected the PCA features in training the SVM classifier for classifying between cavity and the other three tissues, the 5 TIC features in classifying the normal tissue and blood vessels

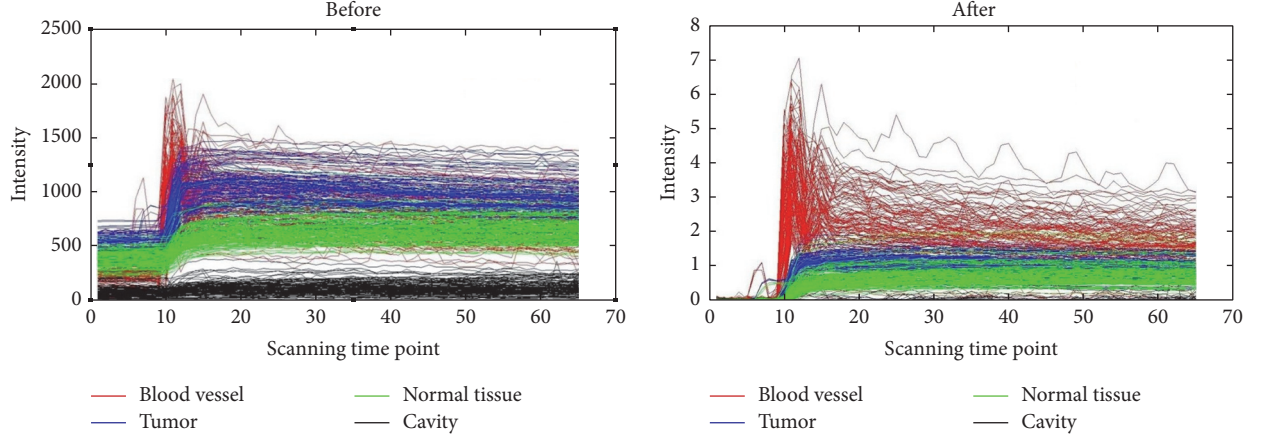


FIGURE 1: The time-intensity curve (TIC) of four regions before and after normalization.

from the other tissues. The radial basis function (RBF) kernel was used in libsvm. The parameters of C and g in libsvm 3.17 were selected by cross-validation and the grid-search technique.

2.3.2. SVM Testing. Before segmentation, a rectangular ROI was roughly drawn in each of the 40 testing samples. We then applied the three trained classifiers to these ROIs for voxel-by-voxel classification. First, the voxels of vessels were classified by the first classifier. Then the voxels in cavity were also classified by the second classifier. Finally, the voxels in normal tissues were also classified. We removed all the voxels classified above, and thus the tumor lesions were ultimately segmented.

To evaluate the segmentation performance of our method, we compared the automated segmentation results with the ground truth and calculated the area overlap measure (AOM) as

$$\text{AOM} = \frac{A_R \cap A_G}{A_R \cup A_G}, \quad (8)$$

where A_R is the segmentation results and A_G is the ground truth. Again, the ground truth for the tumor lesions in these 40 testing samples was manually drawn by an experienced radiologist (Dr. Wei Deng) and double-checked by another experienced radiologist with 14 years' experience who was blind to our study.

To evaluate the superiority of our proposed method to other studies, the corresponding ratio (CR) and percent match (PM) were also calculated as

$$\text{CR} = \frac{\text{TP} - 0.5 \times \text{FP}}{\text{GT}} \times 100\%, \quad (9)$$

$$\text{PM} = \frac{\text{TP}}{\text{GT}} \times 100\%,$$

where true positive (TP) denotes the correctly identified tumor region, false positive (FP) denotes the tumor lesion that was incorrectly predicted as nontumor tissue, and the

ground truth (GT) denotes the correct tumor region drawn by the radiologist. We repeated the above training and testing for 10 times in order to calculate the mean value of AOM, CR, and PM.

3. Results

The unnormalized and normalized TICs of four different regions of one sample were shown in Figure 1. As shown, after normalization, the TICs of different regions were well distinguished between each other. Figure 2(a) shows the average original TICs of different regions in a typical training sample, and Figure 2(b) shows the two components selected by PCA.

HNC tumor segmentation by using the proposed method was successfully performed on the 40 testing samples. The mean AOM was 0.76 with standard deviation of 0.08. Figure 3 shows four typical cases of HNC lesion segmentation, including the ground truth in Figure 3(a) and the automated segmentation results in Figures 3(b)–3(e).

The comparison of segmentation performance between our method and the similar studies is summarized in Table 1. By our method, the mean CR was $79 \pm 9\%$, and the mean PM was $86 \pm 8\%$, which were both higher than those in the previous studies.

4. Discussion

In this study, a SVM-based method for tumor segmentation in DCE-MRI images of HNC was proposed. Experimental results indicated that this proposed method could effectively segment HNC lesions with high accuracy. We achieved an average AOM of 0.76 ± 0.08 . Compared with the SVM-based method proposed in the previous studies [7], the CR value of $79 \pm 9\%$ ($72 \pm 6\%$) and the PM value $86 \pm 8\%$ ($79 \pm 7\%$) in our study were both higher. Compared with other methods about HNC tumor segmentation [5–7], our method also showed higher CR and PM values.

There may be several reasons for better performance of our method. Firstly, the normalized TICs makes the

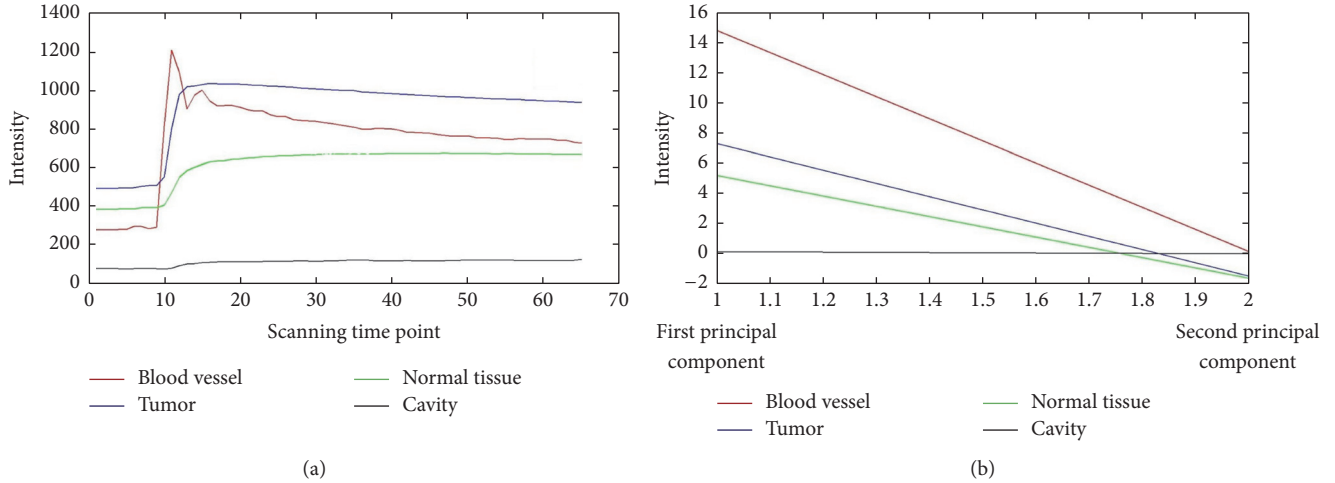


FIGURE 2: The average original time-intensity curves (TICs) of different subregions in a region of interest (ROI) and the two components extracted by using Principal Component Analysis (PCA). (a) The average TICs of different regions. (b) The two components selected by PCA of the normalized TIC.

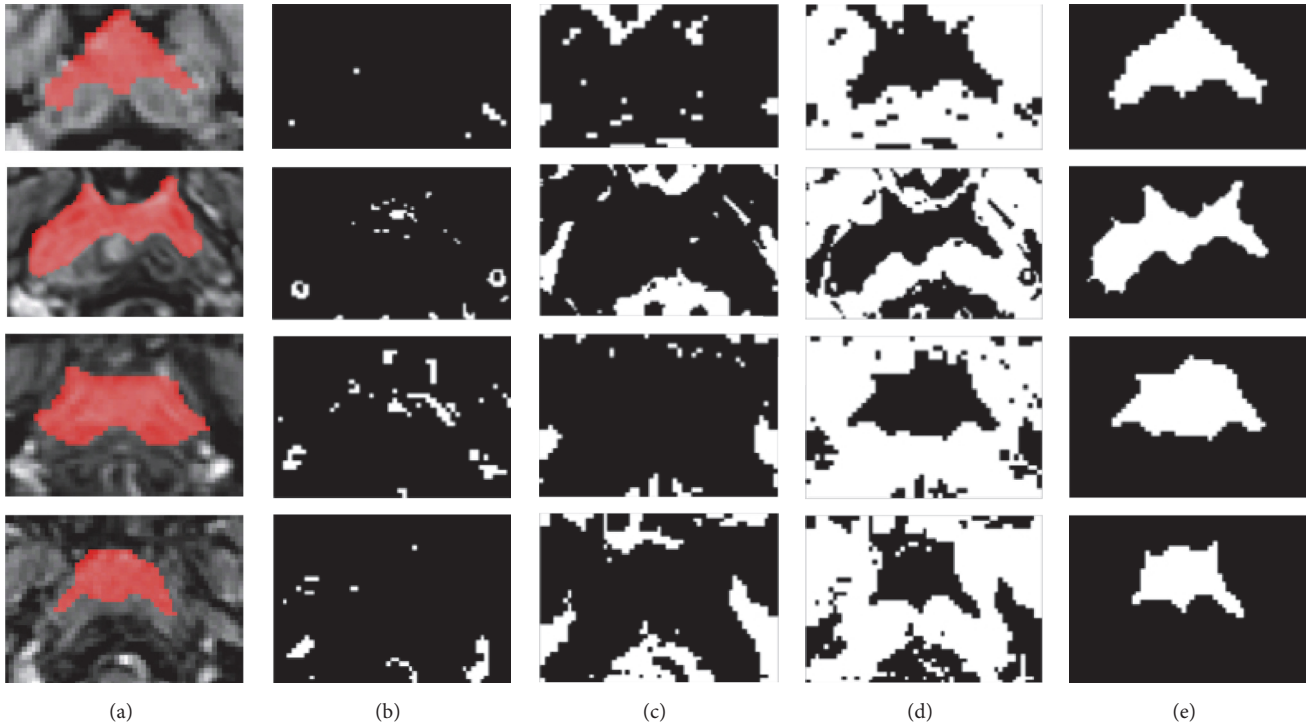


FIGURE 3: Examples of tumor segmentation results from four patients versus the ground truth. Row-wise, from top to bottom, corresponding to 4 typical samples with AOM of 0.89, 0.79, 0.67, and 0.71, respectively. (a) Ground truth of the tumor drawn by an experienced radiologist (in red); (b) the blood vessels identified by the first classifier (in white); (c) the cavity identified by the second classifier (in white); (d) the normal tissue identified by the third classifier (in white); (e) the tumor region (in white) segmented by removing the voxels identified in (b), (c), and (d) from the region of interest (ROI).

data dimensionless and comparable. As shown in Figure 1, before normalization, the TICs of different tissues especially blood vessel and tumor region are similar, while, after normalization, they are well distinguished and meanwhile the differences of TIC are more obvious.

In addition, the extraction and selection of features are essential in segmentation tasks. We chose the features by

using PCA and the features of TIC change for the three classifiers. On the one hand, we found that the classification performance of the PCA features in cavity was more obvious. As shown in Figure 2, by PCA, although only two principal components are shown, the differences in curve variation are still obvious and the computational expense is reduced. On the other hand, we believed that the combination of different

TABLE 1: Comparisons of PM and CR between the segmentation performance obtained by the proposed SVM method and other methods in literature.

Studies	Algorithm	CR ^a	PM ^b
Huang et al. [5]	HMRFC	0.72	0.85
Ritthipravat et al. [6]	Probabilistic Function	0.52	0.85
Zhou et al. [7]	SVM ^d	0.72 ± 0.06	0.79 ± 0.07
Our proposed method	SVM	0.79 ± 0.09	0.86 ± 0.08

^aCorresponding ratio. ^bPercent match. ^cHidden Markov random field. ^dSupport vector machine.

SVM classifiers with different features improves the accuracy of segmentation. In our method with three SVM classifiers, blood vessel, cavity, and normal tissue have been classified independently and successively (as shown in Figure 3). As a supervised learning algorithm, SVM has shown a strong learning ability [4]; thus, with more training samples, the classification performance can be better.

Our study has several limitations. In fact, there is a thin layer of mucosa membrane around the HNC tumor. This tissue might be an obstacle while designing the algorithm based on TIC features, because the TIC is quite similar to the HNC tumor. In the future, we intend to incorporate the high-resolution MRI images for better classification between these two. Another way to improve our method may be the deep learning-based approaches, with which we may obtain more discriminative features and yield improved performance [11].

5. Conclusion

We successfully proposed an automatic segmentation method based on SVM for HNC. The results of this study showed that the segmentation performance was superior to previous studies. Our method, if was further verified with more data, is of potential in the clinical practice of HNC patient management.

Conflicts of Interest

The authors declare that there are no conflicts of interest regarding the publication of this paper.

Authors' Contributions

Wei Deng, Liangping Luo, and Xiaoyi Lin are equal contributors and co-first authors.

Acknowledgments

The study was jointly funded by The National Natural Science Foundation of China (no. 81301273), Shenzhen High-Caliber Personnel Research Funding (no. 000048), and Shenzhen Municipal Scheme for Basic Research (no. JCYJ20160307114900292; no. JCYJ20160608173106220).

References

- [1] W. Deng, "Analysis of the incidence and mortality of nasopharyngeal carcinoma in China between 2003 and 2007," *Tumor*, vol. 32, no. 3, pp. 189–193, 2003.
- [2] A. R. Padhani, "Dynamic contrast-enhanced MRI in clinical oncology: Current status and future directions," *Journal of Magnetic Resonance Imaging*, vol. 16, no. 4, pp. 407–422, 2002.
- [3] C. A. Cuenod and D. Balvay, "Perfusion and vascular permeability: basic concepts and measurement in DCE-CT and DCE-MRI," *Diagnostic and Interventional Imaging*, vol. 94, no. 12, pp. 1187–1204, 2013.
- [4] V. N. Vapnik, "An overview of statistical learning theory," *IEEE Transactions on Neural Networks*, vol. 10, no. 5, pp. 988–999, 1999.
- [5] K.-W. Huang, Z.-Y. Zhao, Q. Gong, J. Zha, L. Chen, and R. Yang, "Nasopharyngeal carcinoma segmentation via HMRFC-EM with maximum entropy," in *Proceedings of the 37th Annual International Conference of the IEEE Engineering in Medicine and Biology Society, EMBC 2015*, pp. 2968–2972, Milan, Italy, August 2015.
- [6] P. Ritthipravat, C. Tatanun, T. Bhongmakapat, and L. Tuntiyatorn, "Automatic segmentation of nasopharyngeal carcinoma from CT images," in *Proceedings of the BioMedical Engineering and Informatics: New Development and the Future - 1st International Conference on BioMedical Engineering and Informatics, BMEI 2008*, pp. 18–22, Sanya, China, May 2008.
- [7] J. Zhou, K. L. Chan, P. Xu, and V. F. H. Chong, "Nasopharyngeal carcinoma lesion segmentation from MR images by support vector machine," in *Proceedings of the 2006 3rd IEEE International Symposium on Biomedical Imaging: From Nano to Macro*, pp. 1364–1367, Arlington, VA, USA, April 2006.
- [8] N. F. Haq, P. Kozlowski, E. C. Jones, S. D. Chang, S. L. Goldenberg, and M. Moradi, "A data-driven approach to prostate cancer detection from dynamic contrast enhanced MRI," *Computerized Medical Imaging and Graphics*, vol. 41, pp. 37–45, 2015.
- [9] H. Akbari, L. Macyszyn, X. Da et al., "Pattern analysis of dynamic susceptibility contrast-enhanced MR imaging demonstrates peritumoral tissue heterogeneity," *Radiology*, vol. 273, no. 2, pp. 502–510, 2014.
- [10] H. Abdi and L. J. Williams, "Principal component analysis," *Wiley Interdisciplinary Reviews: Computational Statistics*, vol. 2, no. 4, pp. 433–459, 2010.
- [11] Y. Bengio, A. Courville, and P. Vincent, "Representation learning: a review and new perspectives," *IEEE Transactions on Pattern Analysis and Machine Intelligence*, vol. 35, no. 8, pp. 1798–1828, 2013.

Research Article

PET Imaging of FSHR Expression in Tumors with ^{68}Ga -Labeled FSH1 Peptide

Donghui Pan,¹ Guifeng Liu,² Yuping Xu,^{1,3} Yanting Wang,⁴ Yuanyuan Yue,⁴ Lizhen Wang,¹ Junjie Yan,¹ Xinyu Wang,¹ Runlin Yang,¹ and Min Yang^{1,3}

¹Key Laboratory of Nuclear Medicine, Ministry of Health, Jiangsu Key Laboratory of Molecular Nuclear Medicine, Jiangsu Institute of Nuclear Medicine, Wuxi, Jiangsu 214063, China

²Department of Radiology, China-Japan Union Hospital of Jilin University, Changchun, Jilin 130033, China

³Nanjing Medical University, Nanjing, Jiangsu 210029, China

⁴Zhengzhou University, Zhengzhou, Henan 450001, China

Correspondence should be addressed to Min Yang; yangmin@jsinm.org

Received 29 March 2017; Revised 7 July 2017; Accepted 25 July 2017; Published 23 August 2017

Academic Editor: Shengxian Rao

Copyright © 2017 Donghui Pan et al. This is an open access article distributed under the Creative Commons Attribution License, which permits unrestricted use, distribution, and reproduction in any medium, provided the original work is properly cited.

FSHR is an appealing target for cancer theranostics. Radiolabeled FSH1 and its derivatives have shown potential to in vivo detect FSHR expression. However, moderate labeling yields (~50% nondecay-corrected) may partially limit their wide use. ^{68}Ga is an excellent PET nuclide due to availability, nearly quantitative reaction, and short physical half-life. In this study, ^{68}Ga labeled FSH1 peptide was developed for imaging of FSHR in cancers. In vitro studies and MicroPET imaging were performed in PC-3 prostate tumor model. [^{68}Ga] Ga-NOTA-MAL-FSH1 can be produced within 20 min with $93.2 \pm 2.1\%$ yield and the radiochemical purity was greater than 95%. It showed that [^{68}Ga] Ga-NOTA-MAL-FSH1 possessed FSHR binding affinities. The tracer was stable in PBS and human serum for at least 2 hours. MicroPET imaging revealed that the PC-3 xenografts were clearly visualized and the tumor uptakes were 1.87 ± 0.10 , 1.26 ± 0.06 , and $0.71 \pm 0.10\%$ ID/g at 0.5, 1 h, and 2 h postinjection. The corresponding tumor to blood and tumor to muscle ratios were 1.77 ± 0.70 , 7.94 ± 1.35 , and 10.37 ± 1.16 and 7.42 ± 0.46 , 26.13 ± 2.99 , and 36.40 ± 2.54 , respectively. FSHR binding specificity was also demonstrated by reduced tumor uptake of [^{68}Ga] Ga-NOTA-MAL-FSH1 after coinjecting excess unlabeled FSH1 peptide. The favorable characters of [^{68}Ga] Ga-NOTA-MAL-FSH1 such as convenient synthesis and specific tumor uptake warrant its further investigation for FSHR expression imaging.

1. Introduction

Follicle-stimulating hormone (FSH) is a central hormone in mammalian reproductive biology. It promotes the mature spermatogenesis for men and follicular maturation for women, respectively. FSH receptor (FSHR) is a glycosylated transmembrane protein belonging to the family of G-protein-coupled receptors. In adult humans and animals, low levels of FSHR were expressed only in endothelial cells of ovary and testis [1–4].

Immunostaining showed that FSHR was overexpressed in the vasculatures of various solid tumors including prostate, breast, lung, and ovarian cancer. On the contrary, healthy and nonmalignant inflammatory tissues were always FSHR

negative [5]. These findings imply that the receptor may be a target for cancer detection and image guided cancer surgery. Moreover, the expression level of FSHR correlates strongly with the response of tumors to antiangiogenic therapies. One clinical study in patients found that the FSHR levels in the primary tumors correlated well with the response to antiangiogenic tyrosine kinase inhibitors (sunitinib) [6]. The percentage of FSHR stained vessels of the responsive patients (~60%) was significantly higher than those in the stable or nonresponsive group (~10% and ~7%, resp.). These characteristics render FSHR an attractive choice for tumor theranostics. Using the FSHR-targeting strategy, paclitaxel attached to FSH peptide was loaded into nanoparticles and the compound displayed antitumor effects [7]. Meanwhile,

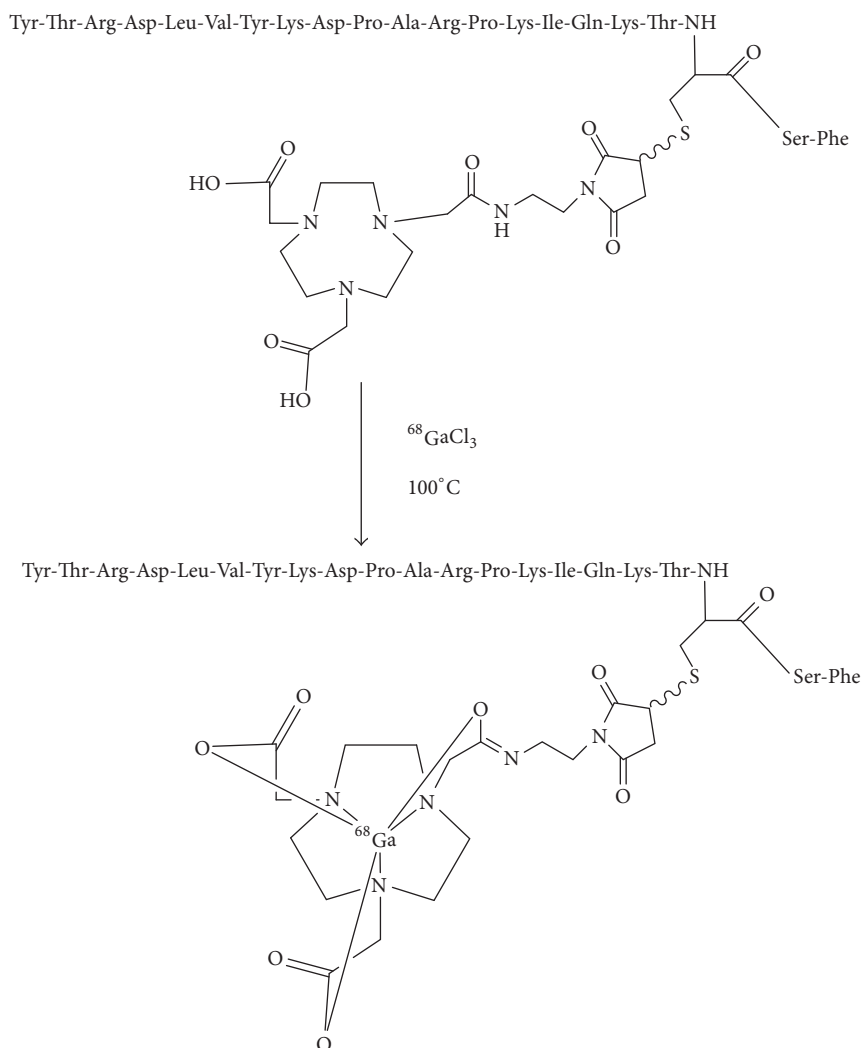


FIGURE 1: Schemes for radiosynthesis of [^{68}Ga] Ga-NOTA-MAL-FSH1.

a nanographene oxide conjugated to a monoclonal antibody against FSHR was successfully developed for targeting delivery of therapeutics [8].

Besides therapy, noninvasive imaging of FSHR is of benefit to monitor biochemical changes and target abundance within a testing subject. Radiolabeled peptides toward receptors have attracted considerable interest for cancer imaging due to fast clearance, high specificity, excellent tissue penetration, and low immunogenicity [9–13]. Preliminary studies revealed that ^{18}F AI labeled FSH1 and its derivatives (FSH2) possessed FSHR binding specificity and might be potential probes to in vivo detect FSHR expression [13, 14]. However, moderate labeling yields (~50% nondecay-corrected) may partially limit their wide use.

Compared with ^{18}F , a metallic positron emitter, ^{68}Ga , can be conveniently obtained from an in-house $^{68}\text{Ge}/^{68}\text{Ga}$ generator and independent of an onsite cyclotron. With a half-life of 68 min, it is also suitable for the pharmacokinetics of many peptides. In addition, biomolecules can be labeled

with ^{68}Ga by nearly quantitative reaction with macrocyclic chelators. It allows possible kit formulation and accelerated the application of the probes [15].

Previous studies showed that the uptake of ^{18}F AI labeled FSH1 in FSHR positive PC-3 xenograft was significantly higher than those of FSH2 counterpart at 1 h postinjection ($2.64 \pm 0.25\%$ ID/g versus $1.88 \pm 0.02\%$ ID/g, resp.). FSH1 peptide may be more suitable for tumor imaging than FSH2 [13, 14]. In this study, FSH1 conjugated to maleimide-NOTA, NOTA-MAL-FSH1, was labeled with ^{68}Ga (Figure 1). The in vitro affinity and the in vivo tumor targeting properties of [^{68}Ga] Ga-NOTA-MAL-FSH1 were also determined in PC-3 tumor models.

2. Materials and Methods

All commercial reagents were of analytical grade. FSH1 peptide was custom made by Apeptide Co., Ltd., (Shanghai, China). NOTA-MAL-FSH1 was synthesized according to the literature and the purity was greater than 95% [13].

The conditions for HPLC system are as follows [16]: A Waters high-performance liquid chromatography (HPLC) system with a Waters 2998 photodiode array detector (PDA) and a preparative C18 HPLC column (5 μm , 250 \times 10 mm, Phenomenex) was used for peptide conjugated purification. The flow is 5 ml/min, and the mobile phase changed from 95% solvent A (0.1% trifluoroacetic acid in water) and 5% solvent B (0.1% trifluoroacetic acid in acetonitrile) (0–2 min) to 35% solvent A and 65% solvent B at 35 min. The UV absorbance was monitored at 218 nm.

The purities of compounds were analyzed by RP-HPLC on a Waters Breeze system equipped with a Radiomatic 610TR flow scintillation analyzer (PerkinElmer) and a Waters 2487 dual λ absorbance detector. A Luna C18 column (5 μm , 250 \times 4.6 mm, Phenomenex) was used at a flow rate of 1 ml/min with the following buffer system: buffer A, 0.1% v/v trifluoroacetic acid in water; buffer B, 0.1% v/v trifluoroacetic acid (TFA) in acetonitrile (ACN); and a gradient of 95% buffer A at 0–2 min to 35% buffer A at 35 min.

The HPLC chromatogram and MS spectrum of NOTA-MAL-FSH1 were listed in Figure 2. MS measured m/z 2968.5 for $[\text{M} + \text{H}]^+$ ($\text{C}_{133}\text{H}_{210}\text{N}_{36}\text{O}_{39}\text{S}$, calculated molecular weight, 2968.1) [13]; ^{68}Ga GaCl_3 was eluted from a $^{68}\text{Ge}/^{68}\text{Ga}$ -generator (ITG, Germany) with 0.05 M HCl. The PC-3 human prostate cancer cell line was purchased from Cell Bank of Shanghai Institutes for Biological Sciences.

2.1. Preparation of ^{68}Ga -NOTA-MAL-FSH1. The fresh ^{68}Ga GaCl_3 (185 MBq) was added to 300 μL 1 M HEPES buffer and followed 20 μg of NOTA-MAL-FSH1 (6.7 nmol) in 10 μL 0.2 M sodium acetate buffer (pH = 4). The mixture was incubated at 100°C for 10 min. After being diluted with 10 mL of deionized water, the complex was loaded into a Varian BOND ELUT C18 column. The labeled peptide was eluted with 200 μL 10 mM HCl in ethanol. The product was reconstituted in 3 ml saline and passed through a 0.22 μm Millipore filter into a sterile vial. Radiochemical purity was checked with the HPLC system. The retention time for ^{68}Ga -NOTA-MAL-FSH1 was 14.2 min (Figure 3(a)).

2.2. Octanol/PBS Partition Coefficient. To an Eppendorf tube filled with 0.5 mL of the radiolabeled peptide (10 μL , 370 KBq) in phosphate-buffered saline (pH 7.4), 0.5 mL of octanol was added. After stirring for 2 min at room temperature, the two layers were separated by centrifugation. Radioactivity in 100 μL of each layer was measured in a γ -counter (Perkin-Elmer), and log D values were calculated [17]. Experiments were performed in triplicate.

2.3. Stability Studies. 10 μL 370 KBq ^{68}Ga Ga -NOTA-MAL-FSH1 in saline was incubated in 200 μL PBS or 200 μL human serum for 30, 60, and 120 min at 37°C, respectively. The stability of the labeled peptide in PBS was determined by directly injecting an aliquot of the solution into the HPLC at the preselected time points.

The serum was first mixed with 200 μL acetonitrile to precipitate the proteins. Subsequently, after centrifugation, supernatant was collected and analyzed by radio-HPLC [18]. Protein-binding fraction was calculated by dividing the

radioactivity of the precipitation layer by the total activity used.

2.4. Cell Lines and Animal Models. PC-3 cells were cultured and grown in F-12 nutrient (Thermo Fisher) mixture supplemented with 10% (v/v) fetal bovine serum at 37°C in an atmosphere containing 5% CO_2 .

The PC-3 tumor model was generated by subcutaneous injection of 5×10^6 cells into the right front flank of male athymic nude mice (4 weeks old, SLAC Laboratory Animal Co., Ltd., China).

The mice were used for MicroPET studies when the tumor volume reached 100–300 mm^3 , which took about 2 weeks. The animal experiments were conducted in compliance with the national regulations and approved by local animal welfare committee.

2.5. Competitive Cell-Binding Assay. To obtain a homogenous mixture, equivalent of $^{\text{nat}}\text{GaCl}_3$ was added to ^{68}Ga Ga -NOTA-MAL-FSH1 and the final solution incubated again for 10 min. Binding affinities toward the FSHR for ^{68}Ga Ga -NOTA-MAL-FSH1 were determined in a competitive binding assay on PC-3 tumor cells using FSH1 as a receptor ligand [19]. PC-3 cells in 6-well plates (2×10^5 cells per well) were cultured until confluency. On the day of assay, cells were washed with binding buffer (RPMI, 0.5% bovine serum albumin). A range of 1 to 5000 nM FSH1 in binding buffer and 370 KBq $^{68/\text{nat}}\text{Ga}$ Ga -NOTA-MAL-FSH1 were added to each well. After incubating at 37°C for 2 h, medium was removed. Then, cells were washed with binding buffer and extracted from the wells by 0.1 M NaOH. Cell-associated radioactivity was determined in a γ -counter (PerkinElmer). Experiments were performed in triplicate. Inhibitory concentration of 50% (IC50) values was determined by GraphPad Prism software (version 5.0).

2.6. Cell Uptakes. PC-3 cells were suspended in 500 μL RPMI 1640 and seeded in 24-well tissues culture plates (1×10^5 cells per well) for overnight incubation. After washing with PBS, the cells were incubated with 370 KBq ^{68}Ga Ga -NOTA-MAL-FSH1 in the presence or absence of unlabeled FSH1 (to a final concentration of 1 μM) at 37°C for 15, 30, 60, and 120 min, respectively. The cells were washed 3 times with ice-cold PBS and lysed in 0.5 mL of 1.0 M NaOH. The remaining radioactivity was measured in the γ -counter. Cell uptakes were expressed as the percentage of added radioactive dose (% AD). Experiments were performed in triplicate.

2.7. MicroPET Imaging. Mice was injected intravenously with 100 μL 3.7 MBq ^{68}Ga Ga -NOTA-MAL-FSH1 in saline under isoflurane anesthesia and subjected to MicroPET imaging. The breathing and body temperature of the mice were monitored by BioVet CT1 system (M2M Imaging Corp.). For the blocking experiment, unlabeled peptide (10 mg/kg body weight) and 3.7 MBq ^{68}Ga Ga -NOTA-MAL-FSH1 were coinjected into five mice. Static PET images were acquired for 5 min using an Inveon MicroPET/CT scanner (Siemens Medical Solutions) at 30 min, 1 h, and 2 h postinjection. The

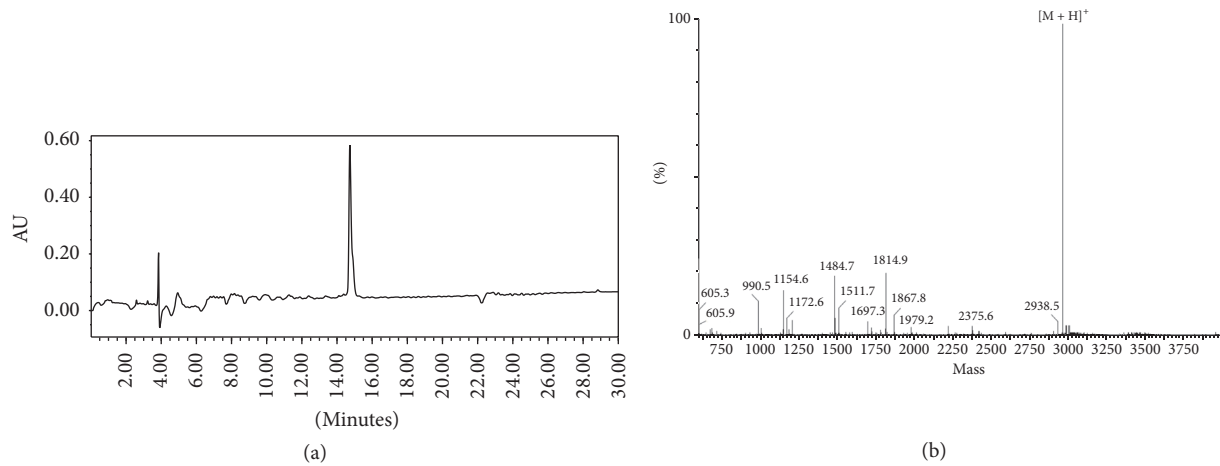


FIGURE 2: HPLC chromatogram (a) and MS spectrum (b) of NOTA-MAL-FSH1.

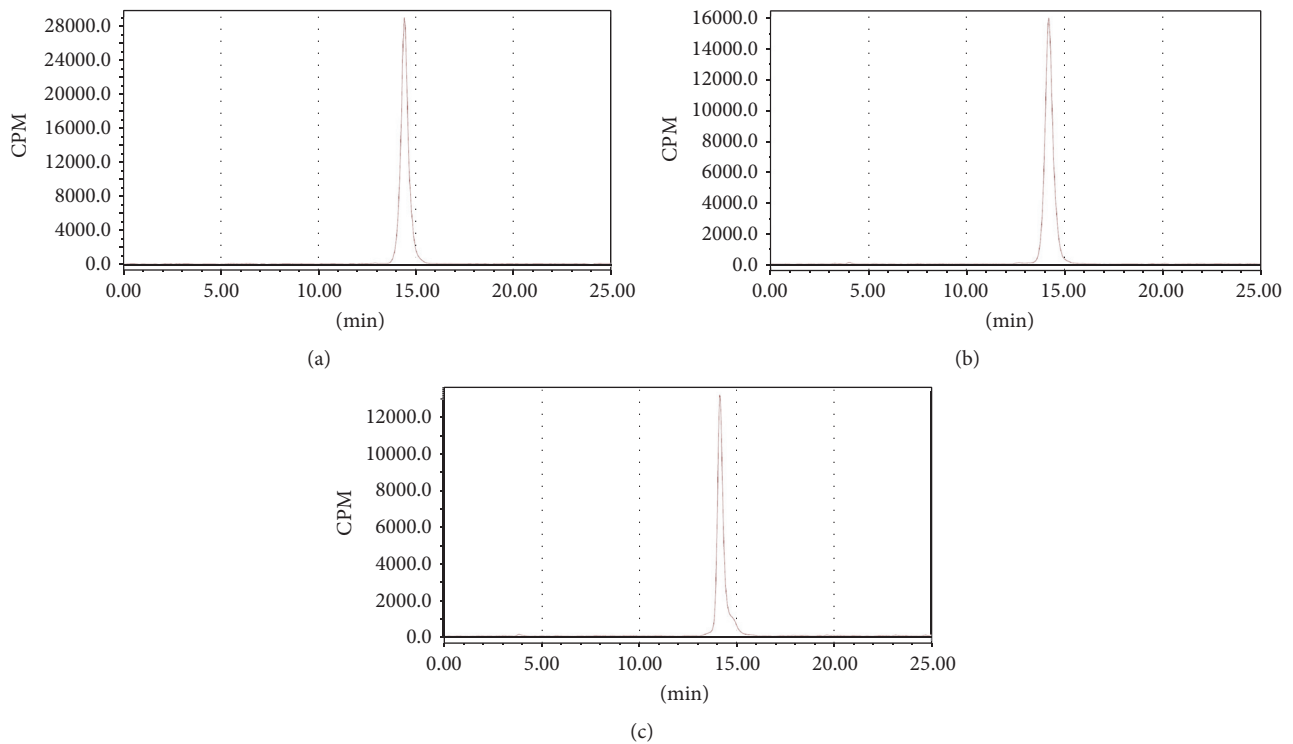


FIGURE 3: HPLC radiochromatogram for (a) purified $[^{68}\text{Ga}]$ Ga-NOTA-MAL-FSH1 and (b) $[^{68}\text{Ga}]$ Ga-NOTA-MAL-FSH1 after 2 h incubation in PBS and (c) $[^{68}\text{Ga}]$ Ga-NOTA-MAL-FSH1 after 2 h incubation in human serum.

quantification analysis of PET images was performed using the same method as previously reported [13].

2.8. Biodistribution Studies. A number of twenty tumor bearing mice were euthanized with isoflurane (inhalation excess) and dissected at 0.5 h, 1 h, and 2 h (5 mice per time-point) after administrating 740 KBq $[^{68}\text{Ga}]$ Ga-NOTA-MAL-FSH1. To determine the specific uptake, mice were co-injected with

the probe with 100 μg of unmodified peptide and sacrificed at 1 h p.i. Normal organs and tumors were collected and weighed. The radioactivity was measured by the γ -counter and the percentage of injected dose per gram of tissue (% ID/g) was determined.

2.9. Statistical Analysis. Statistical analyses were performed using GraphPad Prism (version 5.0). Data were analyzed

TABLE 1: Radiochemical purity (%) of [⁶⁸Ga] Ga-NOTA-MAL-FSH1 after 0.5, 1, and 2 h incubation in PBS and human serum, respectively.

Medium	Time (h)		
	0.5	1	2
PBS	96.7 ± 1.3	97.3 ± 1.2	97.9 ± 1.5
Serum	97.8 ± 0.9	96.9 ± 1.6	96.6 ± 1.1

using the unpaired, 2-tailed Student’s *t*-test. Differences at the 95% confidence level (*p* < 0.05) were considered to be statistically significant.

3. Results

3.1. Chemistry and Radiochemistry. The labeling was performed within 20 min, with a decay-corrected yield of 93.2 ± 2.1% (*n* = 5) and a radiochemical purity of more than 95%. The specific activity was determined to be at least 25 GBq/μmol.

3.2. In Vitro Characterization. The in vitro stability of the ⁶⁸Ga labeled tracer was evaluated by incubating in PBS or human serum at 37°C, respectively. Protein-binding fraction was determined to be 16.5 ± 2.5%. The probe displayed high in vitro stability and showed no degradation products or release of ⁶⁸Ga whether in PBS or human serum (Figures 3(b) and 3(c)). The radiochemical purities of [⁶⁸Ga] Ga-NOTA-MAL-FSH1 were greater than 95% after 2 h in vitro incubation (Table 1).

The partition coefficient (log *D*) of [⁶⁸Ga] Ga-NOTA-MAL-FSH1 was determined to be -3.12 ± 0.05.

3.3. Cell-Binding Assay. The binding of [⁶⁸/^{nat}Ga] Ga-NOTA-MAL-FSH1 to the FSHR on PC-3 tumors was inhibited by various concentrations of nonlabeled FSH1, and the IC50 values were 123.7 ± 1.21 nM (Figure 4).

3.4. Cell Uptake. As shown in Figure 5, [⁶⁸Ga] Ga-NOTA-MAL-FSH1 uptakes in PC-3 cells were 1.10 ± 0.15, 1.39 ± 0.20, 1.51 ± 0.19, and 1.52 ± 0.21% AD for incubating at 15, 30, 60, and 120 min at 37°C, respectively. In the presence of blocking agent, the cell uptakes were significantly reduced to 0.30 ± 0.07% AD after incubating at 60 min, indicating the receptor targeting specificity of the probe.

3.5. MicroPET Imaging. Representative coronal MicroPET images of PC-3 tumor bearing mice (*n* = 5 per group) at different times after intravenous injection of 3.7 MBq [⁶⁸Ga] Ga-NOTA-MAL-FSH1 are shown in Figure 6. PC-3 xenografts were visible with high tumor-to-background contrast. The tumor uptake of [⁶⁸Ga] Ga-NOTA-MAL-FSH1 was determined to be 1.87 ± 0.10, 1.26 ± 0.06, and 0.71 ± 0.10% ID/g at 30, 60, and 120 min (Table 2).

High activity accumulation was also observed in the kidney (21.10 ± 3.64% ID/g at 1 h p.i.) which indicated that ⁶⁸Ga labeled peptide was mainly cleared via the urinary

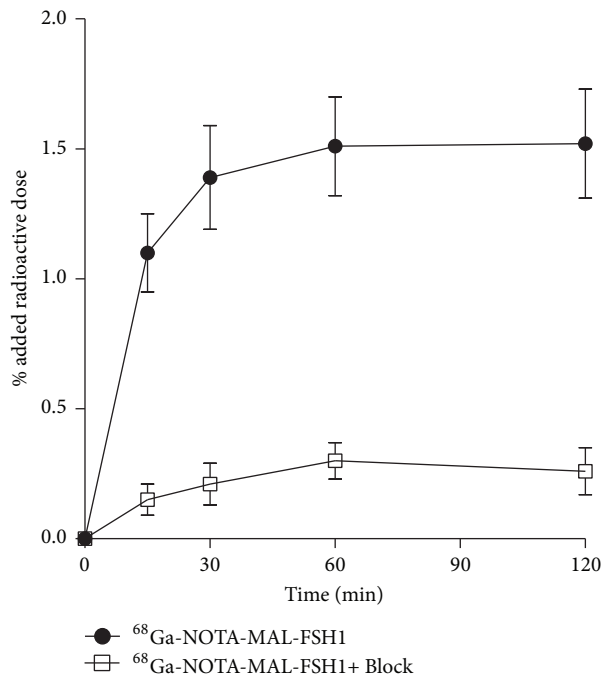


FIGURE 4: Cell uptake assays of [⁶⁸Ga] Ga-NOTA-MAL-FSH1 in PC-3 cells.

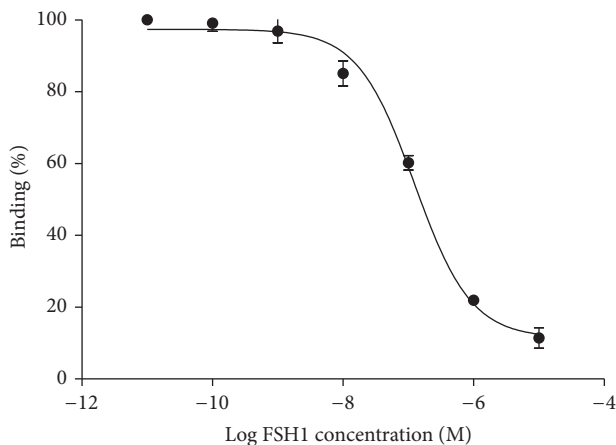


FIGURE 5: Competition of specific bindings of [⁶⁸Ga] Ga-NOTA-MAL-FSH1 with FSH1.

system. The in vivo FSHR binding property of [⁶⁸Ga] Ga-NOTA-MAL-FSH1 was also confirmed by blocking studies. Injection of a large excess of unlabeled FSH1 decreased PC-3 tumor uptakes to 0.31 ± 0.04% ID/g at 1 h postinjection.

3.6. Biodistribution Studies. The results of the biodistribution studies are summarized in Table 3. The tumor uptake of [⁶⁸Ga] Ga-NOTA-MAL-FSH1 was significantly higher than those in the blood and normal organs such as heart, liver, spleen, bone, muscle, and testis at 0.5 h, 1 h, and 2 h postinjection (*p* < 0.01). Due to longer retention of the tracer in tumor, the tumor to blood and tumor to muscle uptake ratios were 1.77 ± 0.70, 7.94 ± 1.35, and 10.37 ± 1.16 and 7.42 ± 0.46, 26.13 ± 2.99, and 36.40 ± 2.54, respectively.

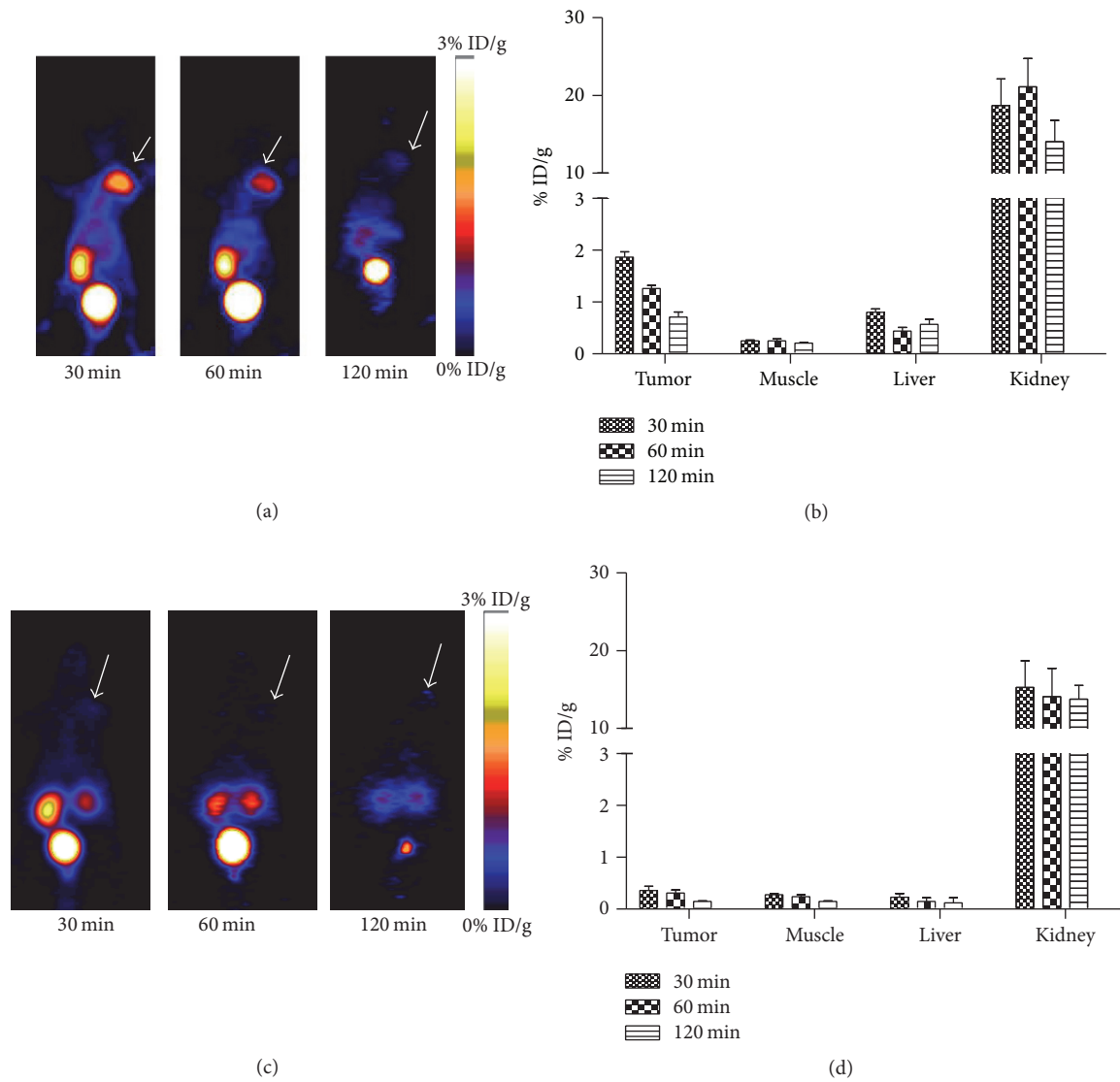


FIGURE 6: In vivo PET imaging of PC-3 xenografted mice with ^{68}Ga Ga-NOTA-MAL-FSH1. Decay-corrected whole-body coronal MicroPET images of PC-3 tumor bearing mice at 30, 60, and 120 min after injection of 3.7 MBq ^{68}Ga Ga-NOTA-MAL-FSH1 without (a) and with (c) blocking dose. Tumors are indicated by arrows. Quantification of ^{68}Ga Ga-NOTA-MAL-FSH1 in PC-3 tumor, liver, kidneys, and muscle without (b) and with (d) blocking dose. ROIs are shown as mean % ID/g \pm SD.

TABLE 2: Radioactivity accumulation (data obtained from MicroPET) in selected organs of PC-3 tumor bearing nude mice after injection of ^{68}Ga Ga-NOTA-MAL-FSH1 at different time points ($n = 5/\text{group}$, mean \pm SD).

Uptake (% ID/g)	^{68}Ga Ga-NOTA-MAL-FSH1			^{68}Ga Ga-NOTA-MAL-FSH1 block		
	0.5 h	1 h	2 h	0.5 h	1 h	2 h
Tumor	1.87 \pm 0.10	1.26 \pm 0.06	0.71 \pm 0.10	0.36 \pm 0.08	0.31 \pm 0.04	0.15 \pm 0.03
Muscle	0.25 \pm 0.02	0.21 \pm 0.04	0.13 \pm 0.03	0.28 \pm 0.09	0.24 \pm 0.03	0.11 \pm 0.01
Liver	0.80 \pm 0.07	0.44 \pm 0.06	0.57 \pm 0.12	0.23 \pm 0.07	0.15 \pm 0.03	0.12 \pm 0.06
Kidney	18.69 \pm 3.44	21.10 \pm 3.64	14.05 \pm 2.76	15.27 \pm 2.89	14.10 \pm 3.01	13.78 \pm 1.96

TABLE 3: Biodistribution of [^{68}Ga] Ga-NOTA-MAL-FSH1 in PC-3 tumor bearing mice at various times after injection ($n = 5$).

Parameter	30 min	60 min	120 min	60 min block
% ID/g in				
Blood	0.95 \pm 0.01	0.17 \pm 0.02	0.13 \pm 0.06	0.19 \pm 0.30
Brain	0.07 \pm 0.01	0.03 \pm 0.01	0.02 \pm 0.01	0.03 \pm 0.01
Heart	0.35 \pm 0.18	0.14 \pm 0.05	0.05 \pm 0.03	0.14 \pm 0.05
Liver	0.93 \pm 0.28	0.56 \pm 0.04	0.37 \pm 0.05	0.12 \pm 0.02
Spleen	0.33 \pm 0.03	0.26 \pm 0.08	0.11 \pm 0.05	0.15 \pm 0.13
Lung	0.67 \pm 0.07	0.14 \pm 0.01	0.10 \pm 0.01	0.17 \pm 0.05
Kidney	24.98 \pm 1.77	18.18 \pm 2.81	13.91 \pm 0.83	15.26 \pm 1.20
Stomach	0.40 \pm 0.17	0.16 \pm 0.06	0.04 \pm 0.01	0.18 \pm 0.08
Intestine	0.32 \pm 0.06	0.15 \pm 0.03	0.05 \pm 0.02	0.20 \pm 0.02
Muscle	0.26 \pm 0.01	0.07 \pm 0.01	0.04 \pm 0.02	0.10 \pm 0.02
Pancreas	0.94 \pm 0.13	0.11 \pm 0.03	0.04 \pm 0.02	0.19 \pm 0.04
Testis	0.24 \pm 0.02	0.08 \pm 0.01	0.03 \pm 0.01	0.06 \pm 0.00
Fat	0.40 \pm 0.01	0.13 \pm 0.06	0.04 \pm 0.00	0.17 \pm 0.15
Bone	0.34 \pm 0.06	0.15 \pm 0.07	0.06 \pm 0.02	0.16 \pm 0.07
Tumor	1.97 \pm 0.17	1.20 \pm 0.27	0.97 \pm 0.15	0.35 \pm 0.12
Ratio of tumor to				
Blood	1.77 \pm 0.70	7.94 \pm 1.35	10.37 \pm 1.16	1.54 \pm 0.07
Muscle	7.42 \pm 0.46	26.13 \pm 2.99	36.40 \pm 2.54	1.95 \pm 0.23
Liver	2.67 \pm 0.50	3.10 \pm 0.40	2.84 \pm 0.90	3.09 \pm 0.24
Intestine	6.68 \pm 1.41	11.21 \pm 2.42	14.17 \pm 1.47	1.74 \pm 0.09
Kidney	0.07 \pm 0.01	0.10 \pm 0.02	0.06 \pm 0.00	0.02 \pm 0.01

Coinjection of excess FSH1 along with [^{68}Ga] Ga-NOTA-MAL-FSH1 resulted in significantly reduced radioactivity accumulation in tumor from 1.20 \pm 0.27% ID/g to 0.35 \pm 0.12% ID/g at 1 h postinjection.

4. Discussion

The recent introduction of ^{68}Ga PET imaging into clinical practice represents a landmark in the ongoing developments in functional and metabolic imaging that is independent of the availability of a cyclotron [20]. Site-specific labeling is important as it provides chemically uniform radioconjugates with well-defined in vivo properties. Maleimide-NOTA is a NOTA-derivatized chelating system, which has specific reactivity toward thiol group [20]. In this study, NOTA-MAL was conjugated to the cysteine residue of FSH1 for site-specific labeling.

Previous studies have documented the overexpression of FSHR in human prostate cancer tissues, particularly in relation to hormone-resistant prostate tumors [9]. Human prostate cancer PC-3 is a hormone-resistant prostate tumor. Thus the characteristics of [^{68}Ga] Ga-NOTA-MAL-FSH1 were preliminary investigated in a PC-3 tumor model.

[^{68}Ga] Ga-NOTA-MAL-FSH1 could be achieved in about 20 min through solid-phase extraction with satisfactory radiochemical purity. Our previous studies showed that the radiolabeling yields of ^{18}F AI labeled FSH1 and its derivatives, FSH2, were 48.6 \pm 2.1% and 41.46 \pm 10.36% (nondecay-corrected), respectively, after 30 min preparation. After decay-corrected determination, the labeling yield of ^{18}F AI

labeled FSH1 and its derivatives was 58.6 \pm 2.5% and 50.5 \pm 11.2%, respectively. Compared with them, the decay-corrected labeling yield (\sim 90%) of [^{68}Ga] Ga-NOTA-MAL-FSH1 was significantly higher than those of ^{18}F AI labeled counterpart [13, 14].

The radiolabeled NOTA-MAL-FSH1 was hydrophilic as indicated by the negative partition coefficients, which is similar to those of ^{18}F AI labeled FSH1 (-3.12 ± 0.05 versus -3.05 ± 0.16 , resp.). [^{68}Ga] Ga-NOTA-MAL-FSH1 showed in vitro stability in human serum and PBS for at least 2 hours.

The IC50 values of displacement [^{68}Ga] Ga-NOTA-MAL-FSH1 with FSHR antagonist, FSH1, were similar to ^{18}F AI labeled counterparts, which primarily indicated the affinity of the tracer for FSHR was retained (123 nM versus 252 nM, resp.). In vitro cell uptake assays also showed that coincubation with excess unlabeled FSH1 significantly blocked tumor uptake demonstrating the receptor binding specificity of the PET probe.

After labeling with ^{68}Ga , we first performed MicroPET scans for [^{68}Ga] Ga-NOTA-MAL-FSH1 in the PC-3 prostate tumor xenograft model. The tracer showed prominent uptakes in the tumor compared with normal tissues such as heart, brain muscle, and livers except kidneys. It was also noted that the uptake values in PC-3 xenografts were slightly lower than those of ^{18}F AI labeled FSH1 (1.26 \pm 0.06% ID/g versus 2.53 \pm 0.20% ID/g at 60 min p.i., resp., $p < 0.05$) [13]. The detailed mechanism was under investigation.

The results of the biodistribution study were consistent with the findings of PET imaging. It showed clear reduction of the radioactivity in the normal organs. The muscle uptakes

of the probe were slightly lower than those of ^{18}F AI-NOTA-MAL-FSH1 (0.07 ± 0.01 versus $0.15 \pm 0.04\%$ ID/g at 1 h p.i., resp.). The resulting tumor to muscle uptake ratio of the probe was more favorable than those of ^{18}F AI labeled FSH1 peptides (26.13 ± 2.99 versus 16.17 ± 3.29 at 1 h p.i., resp.) [13]. It indicated that ^{68}Ga labeled agent might be an alternative to ^{18}F AI labeled compounds for PET imaging of FSHR expression where a cyclotron is of limited access.

The FSHR specificity of [^{68}Ga] Ga-NOTA-MAL-FSH1 was also confirmed by effective tumor uptake inhibition in the presence of excess FSH1 in both noninvasive PET imaging and biodistribution studies. The blocking study suggested that the tumor uptake of the tracer was specific to FSHR.

5. Conclusion

In summary, we have successfully developed a radiolabeled tracer, [^{68}Ga] Ga-NOTA-MAL-FSH1 with high yield and purity. Preclinical data indicates that [^{68}Ga] Ga-NOTA-MAL-FSH1 is promising for noninvasive visualization of FSHR expression in vivo. Further investigation of this novel radiotracer for detection of other FSHR tumor models such as breast and ovarian cancers is currently underway.

Conflicts of Interest

The authors declare no competing financial interests.

Authors' Contributions

Guifeng Liu equally contributed to the work.

Acknowledgments

This work was partially supported by National Natural Science Foundation (81401450, 51473071, 81472749, 21504034, 21401084, and 31671035), Jiangsu Province Science and Technology Foundation (BE2014609, BE2016632, and BK20170204), and Jiangsu Provincial Medical Innovation Team (H201529 and Q201406).

References

- [1] N. S. MacKlon and B. C. J. M. Fauser, "Follicle development during the normal menstrual cycle," *Maturitas*, vol. 30, no. 2, pp. 181–188, 1998.
- [2] M. Simoni, J. Gromoll, and E. Nieschlag, "The follicle-stimulating hormone receptor: biochemistry, molecular biology, physiology, and pathophysiology," *Endocrine Reviews*, vol. 18, no. 6, pp. 739–773, 1997.
- [3] B. Vannier, H. Loosfelt, G. Meduri, C. Pichon, and E. Milgrom, "Anti-human FSH receptor monoclonal antibodies: Immunochemical and immunocytochemical characterization of the receptor," *Biochemistry*, vol. 35, no. 5, pp. 1358–1366, 1996.
- [4] K. Papadimitriou, P. Kountourakis, A. E. Kottorou et al., "Follicle-Stimulating Hormone Receptor (FSHR): A Promising Tool in Oncology?" *Molecular Diagnosis and Therapy*, vol. 20, no. 6, pp. 523–530, 2016.
- [5] A. Radu, C. Pichon, P. Camparo et al., "Expression of follicle-stimulating hormone receptor in tumor blood vessels," *The New England Journal of Medicine*, vol. 363, no. 17, pp. 1621–1630, 2010.
- [6] M. A. Siraj, C. Pichon, A. Radu, and N. Ghinea, "Endothelial follicle stimulating hormone receptor in primary kidney cancer correlates with subsequent response to sunitinib," *Journal of Cellular and Molecular Medicine*, vol. 16, no. 9, pp. 2010–2016, 2012.
- [7] C. W. Lee, L. Guo, D. Matei, and K. Stantz, "Development of follicle-stimulating hormone receptor binding probes to image ovarian xenografts," *Journal of Biotechnology & Biomaterials*, vol. 05, no. 03, 2015.
- [8] D. Yang, L. Feng, C. A. Dougherty et al., "In vivo targeting of metastatic breast cancer via tumor vasculature-specific nanographene oxide," *Biomaterials*, vol. 104, pp. 361–371, 2016.
- [9] H. Hong, Y. Yan, S. Shi et al., "PET of follicle-stimulating hormone receptor: Broad applicability to cancer imaging," *Molecular Pharmaceutics*, vol. 12, no. 2, pp. 403–410, 2015.
- [10] C. D. A. Ferreira, L. L. Fuscaldi, D. M. Townsend, D. Rubello, and A. L. B. D. Barros, "Radiolabeled bombesin derivatives for preclinical oncological imaging," *Biomedicine and Pharmacotherapy*, vol. 87, pp. 58–72, 2017.
- [11] J. Shi, F. Wang, and S. Liu, "Radiolabeled cyclic RGD peptides as radiotracers for tumor imaging," *Biophysics Reports*, vol. 2, no. 1, pp. 1–20, 2016.
- [12] X. Sun, Y. Li, T. Liu, Z. Li, X. Zhang, and X. Chen, "Peptide-based imaging agents for cancer detection," *Advanced Drug Delivery Reviews*, 2016.
- [13] L. Bodei, D. J. Kwekkeboom, M. Kidd, I. M. Modlin, and E. P. Krenning, "Radiolabeled Somatostatin Analogue Therapy Of Gastroenteropancreatic Cancer," *Seminars in Nuclear Medicine*, vol. 46, no. 3, pp. 225–238, 2016.
- [14] Y. Xu, D. Pan, C. Zhu et al., "Pilot study of a novel ^{18}F -labeled FSHR probe for tumor imaging," *Molecular Imaging and Biology*, vol. 16, no. 4, pp. 578–585, 2014.
- [15] C. Zhu, Q. Xu, D. Pan et al., "Prostate cancer imaging of FSHR antagonist modified with a hydrophilic linker," *Contrast Media and Molecular Imaging*, vol. 11, no. 2, pp. 99–105, 2016.
- [16] L. Lang, W. Li, N. Guo et al., "Comparison study of [^{18}F]AI-NOTA-PRGD2, [^{18}F] FPPRGD2, and [^{68}Ga]Ga-NOTA-PRGD2 for PET imaging of U87MG tumors in mice," *Bioconjugate Chemistry*, vol. 22, no. 12, pp. 2415–2422, 2011.
- [17] I. Dijkgraaf, G. M. Franssen, W. J. McBride et al., "PET of tumors expressing gastrin-releasing peptide receptor with an ^{18}F -labeled bombesin analog," *Journal of Nuclear Medicine*, vol. 53, no. 6, pp. 947–952, 2012.
- [18] D. O. Kiesewetter, N. Guo, J. Guo et al., "Evaluation of an [^{18}F]AI-NOTA analog of exendin-4 for imaging of GLP-1 receptor in insulinoma," *Theranostics*, vol. 2, no. 10, pp. 999–1009, 2012.
- [19] G. Kramer-Marek, D. O. Kiesewetter, L. Martiniova, E. Jagoda, S. B. Lee, and J. Capala, "[^{18}F]FBEM-ZHER2:342-Affibody molecule - A new molecular tracer for in vivo monitoring of HER2 expression by positron emission tomography," *European Journal of Nuclear Medicine and Molecular Imaging*, vol. 35, no. 5, pp. 1008–1018, 2008.
- [20] E. W. Price and C. Orvig, "Matching chelators to radiometals for radiopharmaceuticals," *Chemical Society Reviews*, vol. 43, no. 1, pp. 260–290, 2014.

Research Article

An Individually Optimized Protocol of Contrast Medium Injection in Enhanced CT Scan for Liver Imaging

Shi-Ting Feng,¹ Hongzhang Zhu,¹ Zhenpeng Peng,¹ Li Huang,¹ Zhi Dong,¹
Ling Xu,² Kun Huang,¹ Xufeng Yang,¹ Zhi Lin,¹ and Zi-Ping Li¹

¹Department of Radiology, The First Affiliated Hospital, Sun Yat-sen University, 58th, The Second Zhongshan Road, Guangzhou, Guangdong 510080, China

²Faculty of Medicine and Dentistry, University of Western Australia, Perth, WA, Australia

Correspondence should be addressed to Xufeng Yang; xf.y999@163.com, Zhi Lin; m13802524783@163.com, and Zi-Ping Li; liziping163@163.com

Received 28 December 2016; Revised 26 February 2017; Accepted 29 May 2017; Published 10 July 2017

Academic Editor: Silun Wang

Copyright © 2017 Shi-Ting Feng et al. This is an open access article distributed under the Creative Commons Attribution License, which permits unrestricted use, distribution, and reproduction in any medium, provided the original work is properly cited.

Objective. To investigate the effectiveness of a new individualized contrast medium injection protocol for enhanced liver CT scan. **Methods.** 324 patients who underwent plain and dual phase enhanced liver CT were randomly assigned to 2 groups: G1 ($n = 224$, individualized contrast medium injection protocol); G2 ($n = 100$, standard contrast medium injection with a dose of 1.5 ml/kg). CT values and Δ HU (CT values difference between plain and enhanced CT) of liver parenchyma and tumor-liver contrast (TLC) during hepatic arterial phase (HAP) and portal venous phase (PVP) and contrast medium dose were measured. The tumor conspicuity of hepatocellular carcinoma (HCC) between two groups was independently evaluated by two radiologists. **Results.** The mean contrast medium dose of G1 was statistically lower than that of G2. There were no significantly statistical differences in CT values and Δ HU of liver parenchyma during HAP, TLC values during HAP, and PVP between two groups. The CT values and Δ HU of liver parenchyma during PVP of G2 were significantly higher than those of G1. Two independent radiologists were both in substantial conformity in grading tumor conspicuity. **Conclusion.** Using the individually optimized injection protocol might reduce contrast medium dose without impacting on the imaging quality in enhanced liver CT.

1. Introduction

The use of contrast enhanced computed tomography (CT) with iodinated contrast medium (ICM) has significantly improved the accuracy of imaging diagnosis. The rapid development of CT technologies has led to an increase in world-wide usage of ICM. This also results in an increase in its associated adverse reactions, where contrast-induced nephropathy (CIN) is one of the most concerning adverse effects by far. As early as 2001, M. M. Waybill and P. N. Waybill [1] reported that CIN had become the third leading cause of all hospital-acquired renal insufficiency. Since kidney is the primary organ where ICM is metabolized, higher dose of ICM may cause greater damage to the kidney, hence resulting in higher incidence of CIN [2]. Davidson et al. [3] reported that incidence of CIN proportionally correlates with the contrast medium dose used especially amongst high-risk

populations with preexisting renal insufficiency or diabetic neuropathy.

Therefore, on the premise of ensuring the quality and display capability of CT images, reasonable reduction in contrast medium dose may effectively prevent and reduce the incidence of adverse effects associated with enhanced CT scans. Various methods had been previously proposed to reduce the contrast medium dose, including individualized weight-based protocols [4–8], adjustment on the injection time or flow rate of contrast administration [9–11], and the use of additional saline flush [12–14]. Out of the various options, previous reports had demonstrated that personalized weight-based contrast medium injection protocol is an ideal method to reasonably reduce the injection dose of contrast medium [8].

Personalized patient protocol technology abdomen module is a new intelligent platform, which enables the generation

of individualized contrast medium injection protocol based on patient characteristics (such as weight), contrast medium properties (such as iodine content), and other procedure parameters (such as scan timing). P3T™ (Bayer Healthcare, Berlin, Germany) is designed as an individualized contrast medium injection protocol software adapting the iodine delivery rate and total iodine load based upon a nonlinear relationship between patient weight and scan duration in order to achieve diagnostic attenuation. By using patient weight, scan duration, contrast medium concentration, and timing attributes of a test bolus scan, P3T facilitates customizing injection protocol for each patient and procedure. Previous studies have shown that this customized injection software could lead to diagnostic and comparable attenuation values in the coronary CTA for every individual patient and a more efficient use of contrast medium dose [15, 16]. However, the application of this individually optimized protocol of contrast medium injection in liver imaging has not been evaluated previously.

In this study, we aimed to evaluate whether this new contrast medium injection protocol can reduce the contrast medium dose used in enhanced CT scan for liver imaging without limiting the quality of the images.

2. Materials and Methods

2.1. Patients. This prospective study was conducted in accordance with ethical guidelines for human research and was compliant with the Health Insurance Portability and Accountability Act (HIPAA). The study has been approved by the Institutional Review Board (IRB) or ethical committee. Written informed consent was obtained from all patients in the study.

All patients who underwent liver CT scan in our hospital between January 2013 and December 2015 were included in this study. Exclusion criteria were large liver lesions (diameter > 5 cm), diffuse liver diseases such as cirrhosis (suggestive CT findings include abnormal size and shape of liver and spleen, inhomogeneous liver appearance with regenerating nodules and/or signs of portal vein hypertension [17]) and multiple metastases, postliver resection, severe fatty liver (liver density lower than spleen in unenhanced CT), cardiac insufficiency (Grades II, III, and IV, NYHA), liver insufficiency (liver function Child-Pugh B and C), renal failure (1–5 stages, chronic kidney disease (CKD)), and known allergies to contrast medium. In the end, a total of 324 cases were included.

All patients were randomly assigned to either Group 1 (G1) or Group 2 (G2). 224 patients were randomized into G1, with mean age of 47.7 ± 11.7 years and mean weight of 59.8 ± 10.9 kg; 100 patients were randomized into G2, with mean age of 53.9 ± 12.0 years and mean weight of 61.8 ± 10.4 kg. There were no statistical differences in patient age and weight between G1 and G2 ($P > 0.05$). A total of 38 patients with histopathologically proven hepatocellular carcinoma (HCC) were included in the study. 23 patients (18 male and 5 female; mean age of 63.4 years) were randomized to G1 and 15 patients (13 male and 2 female; mean age of 58.3 years) to G2.

2.2. CT Scan Protocols. All patients were scanned using a 64-detector row CT machine (Aquilion 64, Toshiba Medical System, Tokyo, Japan) using same scanning parameters as follows: tube voltage, 120 kV; tube current, 250 mAs; rotation time, 0.358 s; field of view, 400 mm; reconstruction interval, 1 mm; slice thickness, 0.8 mm. All patients underwent both unenhanced and enhanced CT scans during hepatic arterial phase (HAP) and portal venous phase (PVP). According to Muhl et al. and Tu et al. [16, 17], all the enhanced CT scans during HAP and PVP in the present study started at 35 s and 65 s, respectively, after the contrast injection, from the level of diaphragm to inferior hepatic edge. Both groups received the same contrast medium with an iopromide concentration of 300 mgI/mL (Ultravist, Bayer, Germany) injected at a flow rate of 3 mL/s. G1 adopted an individually optimized protocol (P3T abdomen module, Medrad Inc.) of the platform, which automatically calculates the contrast medium dose based on the weight of each patient by using weight factor dosing method calculated from the following formula:

$$\text{Contrast volume (ml)} = \frac{\text{Weight Factor (gI/kg)} * \text{patient Weight (kg)}}{\text{Contrast Concentration (mg/ml)} * 1000} \quad (1)$$

The weight factor is expressed in grams of iodine per kilogram of patient weight and specified as 0.4 gI/kg. Contrast medium concentration is 300 mgI/kg. The formula uses both patient weight and contrast concentration for determining an individualized contrast dose. This module automates the calculation of individualized contrast injection protocols. By providing the patients' weight, iodine concentration, and either the flow rate or duration for the contrast injection protocol, P3T Abdomen will generate a protocol specifically tailor to the patient by delivering customized contrast through weight-based calculation.

According to Megibow et al. [7], acceptable image quality can be obtained for most patients by using low osmolar contrast medium with an iodine concentration of 300 mg/ml given at a dose of 1.5 ml/kg based on body weight. Therefore, in this study, G2 candidates received a standard contrast medium injection protocol with a contrast medium to weight dose of 1.5 ml/kg.

2.3. Quantitative Image Analysis. Quantitative analysis was later performed on the workstation (HP Workstation XW8200, Vitrea 2, Version 3.7). CT values of unenhanced liver parenchyma, CT values of liver parenchyma during HAP and PVP, and CT values of the portal vein during PVP were measured via regions of interest (ROIs) on the axial images. The CT values of liver parenchyma were measured in three liver sections (right anterior, right posterior, and left lateral segments) and the mean values were calculated. The ROI was circular with a fixed area of 0.5 cm^2 . Caution was taken during measurement to avoid the interference of vessels, edges, bile duct, intestine, and so on ROI was placed at the portal vein trunk, and the edges of ROI should be as close as possible to the edge of the vessel wall on both sides of the portal veins. The liver parenchyma enhancement ΔHU

TABLE 1: Results of CT values of liver parenchyma and liver parenchyma Δ HU during HAP and PVP, CT values of portal vein during PVP, and contrast medium dose in G1 and G2.

	CT values of liver parenchyma during HAP (HU)	CT values of liver parenchyma during PVP (HU)	CT values of portal vein during PVP (HU)	Liver parenchyma Δ HU during HAP (HU)	Liver parenchyma Δ HU during PVP (HU)	Contrast medium dose (ml)
G1	77.3 \pm 11.9	102.6 \pm 9.5	147.0 \pm 15.4	21.1 \pm 11.0	46.4 \pm 9.5	78.2 \pm 12.8
G2	76.0 \pm 11.5	106.4 \pm 11.3	159.7 \pm 18.4	18.5 \pm 10.7	49.0 \pm 10.2	93.0 \pm 15.0
<i>P</i>	0.367	0.001	<0.001	0.059	0.021	<0.001

during HAP and PVP was defined as the difference in CT values of liver parenchyma during HAP and PVP compared to unenhanced CT values, respectively.

Tumor-liver contrast (TLC) was used to represent the tumor conspicuity of lesions during HAP and PVP. TLC was previously defined by Baron [18] as the conspicuity of a hepatic tumor expressed by the attenuation difference between the tumor and the hepatic parenchyma. According to Yanaga et al. [19], an attempt was made to maintain a constant ROI area of approximately 2 cm² within the range of 0.8–2.0 cm². In the patients with less than three lesions, the mean TLC values were obtained and calculated from all the lesions; in patients with three or more lesions, the mean TLC values was obtained from the average of the three largest lesions.

2.4. Qualitative Image Analysis. CT examinations were performed in both G1 and G2 patients which contained 23 and 15 cases, respectively, of histopathologically proven HCC. The cases were randomly evaluated by two radiologists independently, both with a minimum experience of 15 years specializing in abdominal imaging, both blinded to the clinical data. A three-level grading system was utilized for evaluation: Grade 1, poor (tumor barely shown); Grade 2, fair (tumor is shown but not as clear as Grade 3); and Grade 3, excellent (tumor clearly shown and presence of tumor can be described with confidence). Each case was reviewed independently and image quality grading was assigned accordingly by the consensus of the two radiologists [19].

2.5. Statistical Analysis. Analysis was performed using SPSS (SPSS, Version 13.0, Chicago, IL, USA). The contrast medium dose, the CT values of liver parenchyma during HAP and PVP, the CT values of portal vein during PVP, TLC values, and liver parenchyma Δ HU during HAP and PVP in G1 and G2 were presented as mean \pm standard deviation (SD). These values were further analyzed by two independent samples *t*-test or Wilcoxon rank sum test, depending on the adherence to normal distribution. If statistically significant differences were observed in the contrast medium dose between G1 and G2, the patients in both groups would be further divided into three subgroups based on patient body weight (\leq 50 kg, >50 kg and <65 kg, and \geq 65 kg) where the mean values were further compared between G1 and G2 corresponding subgroups. The Pearson product-moment correlation coefficient or Spearman rank correlation, depending on the adherence

to normal distribution, was used to assess whether linear correlation can be extracted between the contrast medium dose and the liver parenchyma during HAP and PVP and between CT values of the portal vein during PVP between the two groups.

The conformity assessment of visual grade by the two radiologists was subsequently evaluated for interobserver variability using kappa test. The scale of conformity for interobserver agreement according to kappa coefficient was as follows: less than 0.20, poor; 0.21–0.40, fair; 0.41–0.60, moderate; 0.61–0.80, substantial; and 0.81–1.00, almost perfect [20].

3. Results

Normality test showed that the distribution of these data was all skew in G1 and G2, including CT values of liver parenchyma during HAP and PVP, CT values of portal vein during PVP, liver parenchyma Δ HU during HAP and PVP, and contrast medium dose. Thus, Spearman correlation test was used to compare the differences between the two groups.

The anatomical structure of liver (liver parenchyma, blood vessels, etc.) was clearly displayed in G1. No obvious difference was observed in the anatomical structure of liver during HAP and PVP between G1 and G2 through initial visual assessment (Figure 1).

The quantitative measurement of CT values of liver parenchyma during HAP and PVP, CT values of portal vein during PVP, liver parenchyma Δ HU during HAP and PVP, and the contrast medium dose is shown in Table 1. There were no statistical differences in the CT values of liver parenchyma and liver parenchyma Δ HU during HAP between the two groups. However, there were statistically significant differences in CT values of liver parenchyma during PVP, CT values of portal vein during PVP, liver parenchyma Δ HU during PVP, and contrast medium dose required between the two groups (Table 1). The contrast medium dose used in G1 was reduced by an average of 14.8 ml when compared to G2.

The mean contrast medium doses used in the three weight-based subgroups (\leq 50 kg, >50 kg and <65 kg, and \geq 65 kg) were 62.87, 77.17, and 94.05 ml, respectively, for G1, and 71.38, 88.03, and 106.92 ml, respectively, for G2 (Figure 2). Statistical significant differences were observed between the corresponding subgroups of the same weight range in G1 and G2. The contrast medium doses of the three subgroups in G1

TABLE 2: Analysis on the correlation of contrast medium dose with body weight and CT values of liver parenchyma during HAP and PVP in G1 and G2.

		Body weight	CT values of liver parenchyma during HAP	CT values of liver parenchyma during PVP
Contrast medium dose for G1	<i>r</i> value	0.974	-0.517	-0.119
	<i>P</i> value	<0.001	<0.001	0.079
Contrast medium dose for G2	<i>r</i> value	0.983	-0.406	-0.11
	<i>P</i> value	<0.001	<0.001	0.295

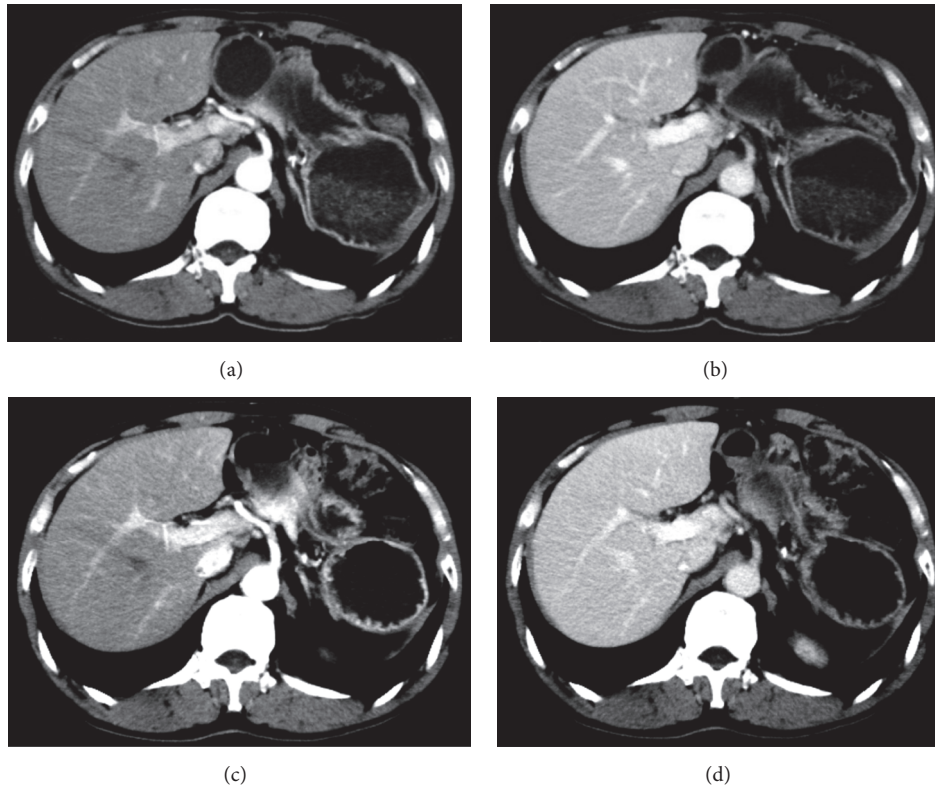


FIGURE 1: The follow-up CT image pairs of a 63-year-old male patient with a body weight of 47 kg after insulin tumor resection. Images (a) and (b) were scanned with injection protocol in G1 (contrast medium dose: 78 ml). The liver parenchyma CT values during HAP and PVP, portal vein CT value during PVP, and liver parenchyma Δ HU during HAP and PVP were 75 HU, 106 HU, 136 HU, 35 HU, and 66 HU, respectively. Images (c) and (d) were scanned with injection protocol in G2 (contrast medium dose: 87 ml). The liver parenchyma CT values during HAP and PVP, portal vein CT value during PVP, and liver parenchyma Δ HU during HAP and PVP were 77 HU, 115 HU, 153 HU, 37 HU, and 75 HU, respectively. The liver anatomical structures of the two pairs of images were both visualized clearly.

were reduced by 8.51, 10.86, and 11.95 ml, respectively, when compared to the corresponding subgroups in G2.

Spearman correlation analysis was adopted to evaluate the correlation of contrast medium dose with CT values of liver parenchyma during HAP and PVP. In G1 and G2, the contrast medium dose was positively correlated with patient weight and CT values of liver parenchyma during HAP (all *P* values were <0.001). On the other hand, no clear correlation was identified between the contrast medium dose and the CT values of liver parenchyma during PVP (G1, *P* = 0.079; G2, *P* = 0.295) (Table 2).

A total of 31 lesions were detected in 23 patients with HCC in G1 with 3 being the highest number of lesions identified in

one single patient. A total of 27 lesions were detected in the 15 patients with confirmed HCC in G2, with 4 being the highest number of lesions identified in one single patient. The TLC values during HAP in G1 and G2 were 20.9 ± 11.8 HU and 19.5 ± 13.2 HU, respectively, and -14.7 ± 14.7 HU and -15.3 ± 16.8 HU, respectively, during PVP (Figure 3). Between the two groups, there were no statistical significant differences demonstrated in the TLC values measured during HAP and PVP (Figure 4). The mean scores of tumor conspicuity of HCC lesions during HAP for G1 and G2 were 2.61 and 2.57, respectively, measured by one radiologist, and 2.47 and 2.53, respectively, measured by the other. The scores given during PVP for G1 and G2 were 2.13 and 2.17, respectively, by

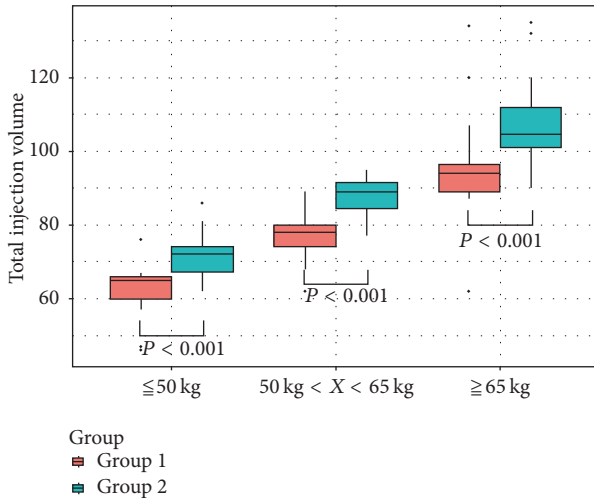


FIGURE 2: The mean contrast medium dose used in the three weight-based subgroups (≤ 50 kg, >50 kg and <65 kg, and ≥ 65 kg) were 62.87, 77.17, and 94.05 ml, respectively, in G1 and 71.38, 88.03, and 106.92 ml, respectively, in G2. There was statistical difference between the subgroups of the same weight range in G1 and G2.

one radiologist and 2.33 and 2.17, respectively, by the other. The two radiologists were both in substantial conformity in grading the tumor conspicuity (G1: κ 0.693, $P < 0.001$; G2: κ 0.734, $P < 0.001$).

4. Discussion

Previous studies have evaluated the image quality of multiphase dynamic enhanced CT of liver using different contrast concentrations [21, 22]. It has been demonstrated by researchers that higher contrast concentrations resulted in better enhancement of liver, where lesions can be more easily identified. However, higher contrast concentration may result in higher osmotic pressure, which can increase the risk of adverse reactions such as contrast-induced nephrotoxicity [23]. Scholars have previously proposed and explored various protocols using fixed abdominal concentration by adjusting contrast medium dose based on body weight. Yamashita et al. [24] used the contrast medium dose of 1.5, 2.0, or 2.5 mL/kg or a fixed dose of 100 mL of iopamidol 300 to determine the optimal contrast dose for helical CT of the abdomen based on patient weight. They found the use of 2.0–2.5 mL/kg of intravenous contrast medium produced best results when compared to 1.5 mL/kg group and fixed dose group. Arana et al. [25] compared 1.75 ml/kg dosing regime and a fixed dose of 120 ml using the same nonionic contrast medium (320 mgI/ml) and found that an injection volume of 1.75 ml/kg offered a more optimal diagnostic quality. Compared to these previous studies, a lower the contrast medium dose was adapted for the injection protocol in this current study.

The individualized contrast injection protocol used in this study offers flexibility by providing the option of three dosing methods: weight factor, volume factor, and iodine load. The primary difference between these dosing methods

lies in the variables (patient weight and concentration) used for calculating individualized contrast medium dose. Weight factor method was used in the present study, in which both patient weight and concentration were used to determine an individualized contrast medium dose. A fixed weight factor and concentration were set as default value for all patients; weight was the only variable required where the platform would then generate an individualized contrast medium injection protocol. Due to its easy-to-use characteristics, this unique optimized contrast medium dosing method provides individualized contrast medium injection protocol for each patient even under special clinical and research requirements.

It is well known that the liver uniquely receives a dual blood supply from the hepatic artery and the portal vein, which approximately contributes 25% and 75% of the total blood supply respectively. The arterial and portal blood mixes within the hepatic sinusoids before draining into the hepatic venous system [26]. Immediately after contrast medium injection, the contrast enhancement of the liver parenchyma is completely provided by the hepatic artery during the early HAP, and then the portal vein becomes involved in the late HAP and will be the major source of blood supply during PVP. Ichikawa et al. [27] reported that, during HAP, the amplitude of the contrast enhancement of well-arterial-perfused organs such as focal hypervascular hepatic lesions was dependent on the injection speed of contrast medium. Furthermore, the injection dose was one of the most important factors in determining the amplitude of the contrast enhancement of poorly arterial-perfused organs, such as the portal vein or liver parenchyma. Although the contrast medium injection dose of the two groups uses different weight-based protocols in this study, the contrast medium injection rate and contrast medium concentration remained fixed and therefore do not contribute to the differences in CT values of liver parenchyma during HAP. Hence, as the body weight increases, there would be a negative correlation between the contrast dose and the CT values of liver parenchyma during HAP in both groups. Moreover, George et al. [8] used 98 ml iodinated contrast medium (300 mgI/ml) delivered at 3 ml/s with the patient being scanned at 60 seconds, and they found statistically significant negative correlation between patient weight and radiodensity at the portal vein, aorta, spleen, and liver. This finding indicated that, as patient weight increases, the degree of enhancement will decrease during PVP when fixed contrast medium dosing regime was applied. However, in the current study, same fixed weight factor (0.4 mgI/kg) and volume factor (1.5 ml/kg) were applied to patients from both groups. Therefore, there was no negative correlation between the contrast dose and the CT values of liver parenchyma during PVP.

Moreover, the liver parenchyma Δ HU (CT value difference between plain and enhanced CT) during PVP decreased with higher body weight, especially in obese patients in this study. However, the liver parenchyma Δ HU during HAP of G1 and G2 did not demonstrate statistical significant differences. As most HCC are supplied by the hepatic arteries, the mass density of HCC lesions generally shows vivid enhancement during HAP. These lesions then become hypodense compared

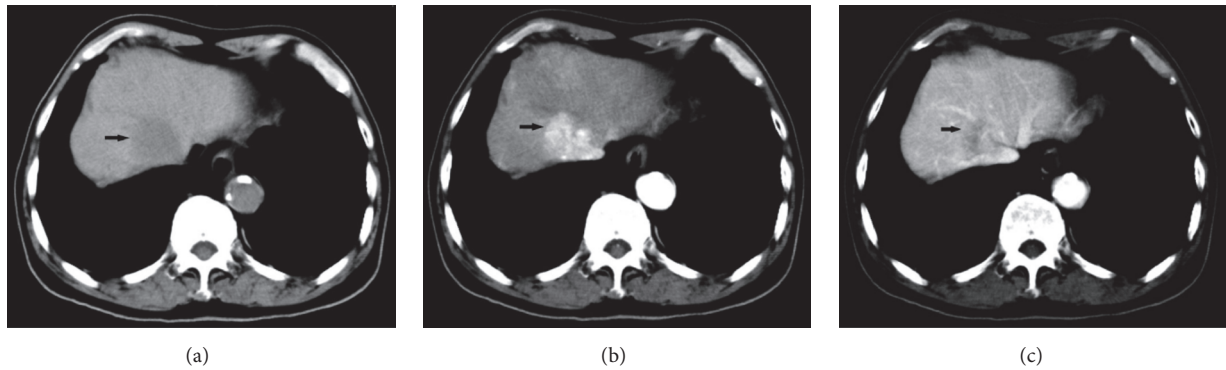


FIGURE 3: A 48-year-old male patient of G1 with HCC lesions was found liver occupied by ultrasound in physical examination. Unenhanced CT scans (a) revealed a liver S7 low-density round mass with clear boundary. Enhanced CT scans revealed significantly enhanced heterogeneous mass during HAP (b), the density of which was higher than the liver parenchyma of the same slice, and TLC value was 38 HU; the mass density in PVP (c) was lower than liver parenchyma and was enhanced during HAP and hypodense during PVP, and TLC value was -12 HU.

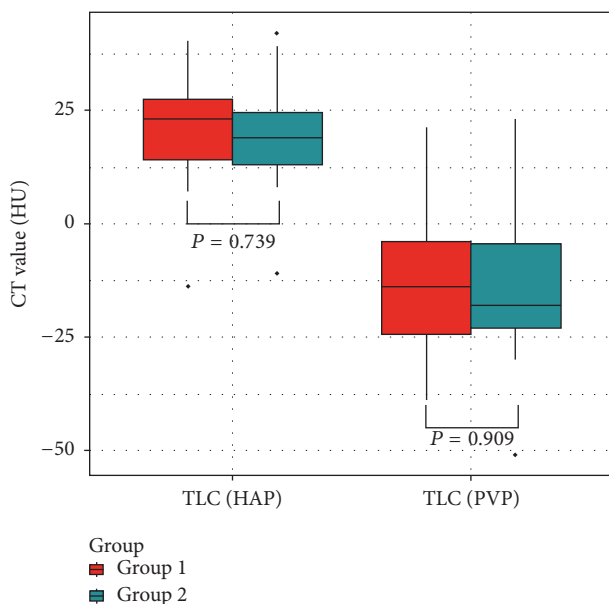


FIGURE 4: No statistical differences were found in the TLC values during HAP and during PVP between the two groups. The TLC values during HAP in G1 and G2 were 20.9 ± 11.8 HU and 19.5 ± 13.2 HU, respectively, while the TLC values during PVP in G1 and G2 were -14.7 ± 14.7 HU and -15.3 ± 16.8 HU, respectively.

to the rest of the normal hepatic parenchyma while the blood was washed out during PVP. Guerrisi et al. [28] founded that, compared to an iodine concentration of 320 mgI/ml, contrast medium with an iodine concentration of 400 mgI/ml would significantly increase the conspicuity of HCC during HAP. Furthermore, Fujigai et al. [29] demonstrated hypervascular HCC could be better depicted during HAP with sufficient hepatic enhancement of 50 HU during delayed phase when a fixed concentration of 320 mgI/ml iodine with the injection plan of 630 mgI/kg was used instead of the contrast medium injection protocol of 525 mgI/kg. In this study, fixed injection speed and optimized contrast medium concentration were used. The scores of tumor conspicuity of HCC during HAP

remained excellent in both groups. Although the contrast medium dose was lower in G1, there were no statistical differences in the CT values of normal liver parenchyma during HAP between the two groups. Furthermore, the TLC values and scores of tumor conspicuity of HCC were also comparable between the two groups. These findings suggest that individualized contrast medium injection protocol has the advantage of reducing contrast dose without significantly affecting the degree of enhancement of normal liver parenchyma and HCC lesions. The enhancement during PVP is also important for the diagnosis and differential diagnosis of liver diseases, especially for certain pathologies which are dependent on portal venous blood supply. As only the cases with normal liver or HCC were enrolled, whether the decrease in the degree of hepatic enhancement during PVP could impact on the diagnosis and differential diagnosis for liver diseases other than HCC remains uncertain. In order to avoid these possible limitations, we suggest incremental increase to the weight factor for obese patients to maintain a steady enhancement effect. However, further studies are required to identify the optimal method in adjusting weight factor safely and efficiently for this group of patients.

There are limitations to the study. Firstly, although body weight is the most important factor affecting the degree of contrast enhancement in liver, others such as heart rate and vascular conditions are also important factors. Therefore, multiple linear regression models should be used in future studies to establish the correlation of CT values of liver parenchyma in dual phases with the contrast medium dose and cardiac output. This will help to evaluate and predict the function and influence of various factors on the contrast enhancement of liver after adjusted contrast medium doses based on body weight are applied. Secondly, patients with diffuse liver disease such as cirrhosis were excluded out in our study. Liver cirrhosis can influence haemodynamics of the liver where the enhancement of the hepatic parenchyma in dynamic CT is different from the normal liver, and the use of individualized contrast medium injection protocol in patient liver cirrhosis becomes difficult to evaluate. Therefore, patients with liver cirrhosis were excluded from this study

- Is it necessary?" *PLoS ONE*, vol. 10, no. 6, Article ID e0128625, 2015.
- [16] C. Muhl, M. Kok, S. Altintas et al., "Evaluation of individually body weight adapted contrast media injection in coronary CT-angiography," *European Journal of Radiology*, vol. 85, no. 4, pp. 830–836, 2016.
- [17] R. Tu, L.-P. Xia, A.-L. Yu, and L. Wu, "Assessment of hepatic functional reserve by cirrhosis grading and liver volume measurement using CT," *World Journal of Gastroenterology*, vol. 13, no. 29, pp. 3956–3961, 2007.
- [18] R. L. Baron, "Understanding and optimizing use of contrast material for CT of the liver," *American Journal of Roentgenology*, vol. 163, no. 2, pp. 323–331, 1994.
- [19] Y. Yanaga, K. Awai, T. Nakaura et al., "Optimal contrast dose for depiction of hypervascular hepatocellular carcinoma at dynamic CT using 64-MDCT," *American Journal of Roentgenology*, vol. 190, no. 4, pp. 1003–1009, 2008.
- [20] H. Svanholm, H. Starklint, H. J. G. Gundersen, J. Fabricius, H. Barlebo, and S. Olsen, "Reproducibility of histomorphologic diagnoses with special reference to the kappa statistic," *APMIS*, vol. 97, no. 8, pp. 689–698, 1989.
- [21] D. V. Sahani, G. Soulez, K. M. Chen et al., "A comparison of the efficacy and safety of iopamidol-370 and iodixanol-320 in patients undergoing multidetector-row computed tomography," *Investigative Radiology*, vol. 42, no. 12, pp. 856–861, 2007.
- [22] J. J. W. Sandstede, A. Werner, C. Kaupert et al., "A prospective study comparing different iodine concentrations for triphasic multidetector row CT of the upper abdomen," *European Journal of Radiology*, vol. 60, no. 1, pp. 95–99, 2006.
- [23] R. Solomon and G. Deray, "How to prevent contrast-induced nephropathy and manage risk patients: practical recommendations," *Kidney international Supplement*, no. 100, pp. S51–53, 2006.
- [24] Y. Yamashita, Y. Komohara, M. Takahashi et al., "Abdominal helical CT: Evaluation of optimal doses of intravenous contrast material - A prospective randomized study," *Radiology*, vol. 216, no. 3, pp. 718–723, 2000.
- [25] E. Arana, L. Martí-Bonmatí, E. Tobarra, and C. Sierra, "Cost reduction in abdominal CT by weight-adjusted dose," *European Journal of Radiology*, vol. 70, no. 3, pp. 507–511, 2009.
- [26] J. E. Skandalakis, L. J. Skandalakis, P. N. Skandalakis, and P. Mirilas, "Hepatic surgical anatomy," *Surgical Clinics of North America*, vol. 84, no. 2, pp. 413–435, 2004.
- [27] T. Ichikawa, S. M. Erturk, and T. Araki, "Multiphasic contrast-enhanced multidetector-row CT of liver: Contrast-enhancement theory and practical scan protocol with a combination of fixed injection duration and patients' body-weight-tailored dose of contrast material," *European Journal of Radiology*, vol. 58, no. 2, pp. 165–176, 2006.
- [28] A. Guerrisi, D. Marin, R. C. Nelson et al., "Effect of varying contrast material iodine concentration and injection technique on the conspicuity of hepatocellular carcinoma during 64-section MDCT of patients with cirrhosis," *British Journal of Radiology*, vol. 84, no. 1004, pp. 698–708, 2011.
- [29] T. Fujigai, S. Kumano, M. Okada et al., "Optimal dose of contrast medium for depiction of hypervascular HCC on dynamic MDCT," *European Journal of Radiology*, vol. 81, no. 11, pp. 2978–2983, 2012.

Research Article

Dynamic Contrast-Enhanced Magnetic Resonance Imaging of Regional Nodal Metastasis in Nasopharyngeal Carcinoma: Correlation with Nodal Staging

Bingsheng Huang,¹ Dora Lai-Wan Kwong,² Vincent Lai,³ Queenie Chan,⁴
Brandon Whitcher,⁵ and Pek-Lan Khong³

¹National-Regional Key Technology Engineering Laboratory for Medical Ultrasound, Guangdong Key Laboratory for Biomedical Measurements and Ultrasound Imaging, School of Biomedical Engineering, Health Science Centre, Shenzhen University, Shenzhen, China

²Department of Clinical Oncology, The University of Hong Kong, Pokfulam, Hong Kong

³Department of Diagnostic Radiology, The University of Hong Kong, Pokfulam, Hong Kong

⁴Philips Healthcare, Sheung Wan, Hong Kong

⁵Mango Solutions, London, UK

Correspondence should be addressed to Pek-Lan Khong; plkhong@hku.hk

Received 28 December 2016; Revised 13 March 2017; Accepted 6 April 2017; Published 29 May 2017

Academic Editor: Ziyue Xu

Copyright © 2017 Bingsheng Huang et al. This is an open access article distributed under the Creative Commons Attribution License, which permits unrestricted use, distribution, and reproduction in any medium, provided the original work is properly cited.

Objective. To determine if the perfusion parameters by dynamic contrast-enhanced magnetic resonance imaging (DCE-MRI) of regional nodal metastasis are helpful in characterizing nodal status and to understand the relationship with those of primary tumor of nasopharyngeal carcinoma (NPC). **Materials and Methods.** Newly diagnosed patients imaged between August 2010 and January 2014 and who were found to have enlarged retropharyngeal/cervical lymph nodes suggestive of nodal disease were recruited. DCE-MRI was performed. Three quantitative parameters, K^{trans} , v_e , and k_{ep} , were calculated for the largest node in each patient. Kruskal-Wallis test was used to evaluate the difference in the parameters of the selected nodes of different N stages. Spearman's correlation was used to evaluate the relationship between the DCE-MRI parameters in nodes and in primary tumors. **Results.** Twenty-six patients (7 females; 25~67 years old) were enrolled. K^{trans} was significantly different among the patients of N stages (N1, $n = 3$; N2, $n = 17$; N3, $n = 6$), $P = 0.015$. Median values (range) for N1, N2, and N3 were 0.24 min^{-1} ($0.17\sim 0.26 \text{ min}^{-1}$), 0.29 min^{-1} ($0.17\sim 0.46 \text{ min}^{-1}$), and 0.46 min^{-1} ($0.29\sim 0.70 \text{ min}^{-1}$), respectively. There was no significant correlation between the parameters in nodes and primary tumors. **Conclusion.** DCE-MRI may play a distinct role in characterizing the metastatic cervical lymph nodes of NPC.

1. Introduction

Nasopharyngeal carcinoma (NPC) is an aggressive head and neck cancer with a high incidence in Southern China including Hong Kong. Accurate staging using the International Union Against Cancer (UICC) tumor-node-metastasis (TNM) staging system is critical for treatment planning and the prediction of patient outcome [1–3]. Regardless of the status of the primary lesion, nodal metastasis is a significant prognostic factor for survival [4]. Hence the accurate

detection and the characterization of metastatic nodes are of paramount importance in NPC patient management.

DCE-MRI is a functional imaging modality that has the potential to characterize perfusion and microcirculation and, thus, may have a role to play as a noninvasive biomarker of cancer. The three quantitative parameters K^{trans} , v_e , and k_{ep} derived by DCE-MRI are frequently used. K^{trans} (in min^{-1}) is the volume transfer constant of contrast agent from blood plasma to extravascular extracellular space (EES) reflecting both blood plasma flow and permeability, v_e is

the volume of EES per unit volume of tissue, and k_{ep} (in minute^{-1}) is the flux rate constant of contrast agent from EES to plasma and equal to K^{trans}/v_e [5]. Studies have found DCE-MRI to be useful in differentiating diseased nodes from normal nodes in head and neck squamous cell cancer, breast cancer, and cervical cancer [6–8]. In these studies, it has been shown that, in malignant nodes, microvascular permeability and the extravascular extracellular space are increased.

In our previous study we have reported the feasibility of applying DCE-MRI in NPC [9]. Our findings suggest that the evaluation of DCE-MRI by both semiquantitative and quantitative methods is useful in characterizing the neovasculature and permeability of NPC tumors. However only primary NPC tumors were studied. In the present study, we have included the evaluation of regional metastatic nodes using DCE-MRI. Since previous studies have reported increased microvascular permeability in tumors or diseased nodes (Padhani et al., 2000; Yao et al., 2011; Chang et al., 2008), we hypothesized that nodal DCE-MRI parameters, which reflect the microvascular permeability in regional metastatic lymph nodes, correlate with nodal stage and the DCE-MRI parameters in the primary tumor which is an indicator of tumor aggressiveness.

2. Materials and Methods

2.1. Patients. This study was approved by the Institutional Review Board of The University of Hong Kong/Hospital Authority Hong Kong West Cluster. All consecutive newly diagnosed NPC patients referred to the MRI Unit at The University of Hong Kong between August 2010 and January 2014 were prospectively included. Patients with presumed metastatic regional lymph nodes, based on enlarged lymph nodes (>1 cm short axis diameter) on MRI, and supported by increased metabolic activity on ^{18}F -FDG PET-CT scans (nodal SUVmax > 2.5) performed within one week of the MRI scans, were included. The final diagnosis of metastatic lymph nodes and the N stage were achieved by both the imaging findings (MRI and PET-CT) and histological results. Written informed consent was obtained for all patients. TNM staging was performed according to the Joint Committee on Cancer (AJCC) staging system [10].

2.2. DCE-MRI Techniques. After routine structural MRI acquisition, DCE-MRI of the nasopharynx and upper neck was performed on a 3.0-T MRI system (Achieva; Philips Healthcare). Four acquisitions were obtained in a chronological order with a field of view (FOV) of $22 \times 22 \times 6$ cm (AP \times RL \times FH): precontrast T_1 -weighted fast field echo (FFE) acquisition using a flip angle of 5° (“FA5” acquisition) in 1 minute 22 seconds; T_2 -weighted imaging (“T2W” acquisition) in 50 seconds; B1 mapping measurement acquisition (“B1MAP” acquisition) in 1 minute 23 seconds; and DCE acquisition using a flip angle of 15° (“FA15” acquisition) in 6 minutes 47 seconds with 65 dynamic scans. The details of scanning protocols have been described in our previous paper [9]. All four acquisitions were performed in the same anatomical region and reconstructed to the same resolution. The contrast agent

Gd-DOTA (Dotarem, Guerbet, France) was injected intravenously as a bolus into the blood at around the 8th dynamic acquisition using a power injector system (Spectris Solaris, MedRad, USA), immediately followed by a 25-mL saline flush at a rate of 3.5 mL per second. The dose of Gd-DOTA was 0.1 mmol/(kg body weight) for each patient.

2.3. Data Analysis. All the acquired DCE-MRI images were used for quantitative analysis, and the parametric maps of K^{trans} , k_{ep} , and v_e were calculated as in our previous publication [9]. The procedure of calculating parametric maps of K^{trans} , k_{ep} , and v_e was performed using the software dcmcriS4 (<http://cran.r-project.org/web/packages/dcmcriS4/>) developed by Whitcher and Schmid [11]: firstly the maps of contrast concentration of 65 time points were calculated from the DCE-MRI images and secondly for each voxel the contrast concentration curve and the population AIF [9] were fitted to the pharmacokinetic model to calculate the maps of the three parameters.

For each patient, since there are usually more than 1 metastatic node, as done in the literature [12–14], the largest metastatic node within the scanned region determined by the sum of long and short of axis was identified by a neuroradiologist (PL Khong) based on conventional anatomical MR images (T_1 -weighted, T_2 -weighted, and postcontrast T_1 -weighted) and treated as the representative node in our study. The node boundary was identified in the relevant consecutive slices of the T_2W images of DCE-MRI scan and a series of two-dimensional regions of interest (ROI) were contoured using the software ImageJ (NIH, USA) (V Lai). The average K^{trans} , k_{ep} , and v_e values in each node were calculated and used for further analysis.

The normality of the DCE-MRI parameters distribution in our cohort was checked using Shapiro–Wilk test. ANOVA (for data of normal distribution) or Kruskal–Wallis test (for data which are not normal distribution) were used to evaluate the difference among tumor N stages. Pearson’s correlation (for data of normal distribution) or Spearman’s correlation (for data which are not normal distribution) was performed to study the correlations between the DCE-MRI parameters in nodes and in primary tumors and between the DCE-MRI parameters in nodes and nodal size. All statistical analyses were performed using SPSS 20 (SPSS Inc, Chicago, IL, USA), and $P < 0.05$ was considered statistically significant.

3. Results

The cohort characteristics of this study are shown in Table 1. A total of 26 patients were included and 7 of them were female. The mean age was 45 years (range, 25–67 years; SD, 12 years). The correlations between the DCE-MRI parameters in nodes and nodal size are insignificant with all P values higher than 0.2.

By Kruskal–Wallis test, K^{trans} in the largest node of each patient was significantly different among the various N stages ($P = 0.015$). Median values and ranges were N1 ($n = 3$), 0.24 min^{-1} and $0.17\sim 0.26 \text{ min}^{-1}$; N2 ($n = 17$), 0.29 min^{-1} and $0.17\sim 0.46 \text{ min}^{-1}$; N3 ($n = 6$), 0.46 min^{-1} and $0.29\sim 0.70 \text{ min}^{-1}$, respectively (Figure 1). k_{ep} and v_e in the largest

TABLE 1: Patient demographic data and tumor characteristics ($N = 26$).

Baseline characteristics	
Age (years)	
Range	25~67
Median	45
Mean \pm SD	45 \pm 12
Sex	
Number of female patients	7
Number of male patients	19
Stage	
T stage	Number of patients
1	10
2	5
3	9
4	2
N stage	Number of patients
1	3
2	17
3	6
M stage	Number of patients
0	25
1	1

Notes. Age (years) is patient age at diagnosis; T, N, and M stages were evaluated according to the American Joint Committee on Cancer (AJCC) staging system.

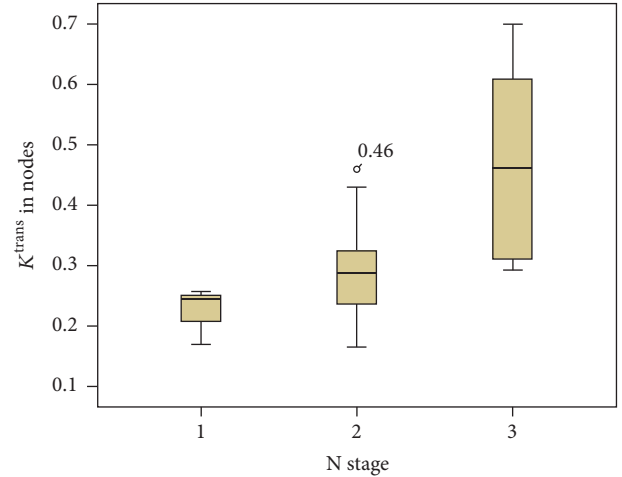
Median values and ranges were N1 ($n = 3$), 0.24 min^{-1} and $0.17\sim 0.26 \text{ min}^{-1}$; N2 ($n = 17$), 0.29 min^{-1} and $0.17\sim 0.46 \text{ min}^{-1}$; N3 ($n = 6$), 0.46 min^{-1} and $0.29\sim 0.70 \text{ min}^{-1}$, respectively (Figure 1). k_{ep} and v_e in the largest node were not correlated with N stage ($P = 0.485$ and 0.113 , resp.). The median values and ranges of k_{ep} were N1, 0.44 min^{-1} and $0.33\sim 0.66 \text{ min}^{-1}$; N2, 0.38 min^{-1} and $0.13\sim 0.67 \text{ min}^{-1}$; N3, 0.36 min^{-1} and $0.10\sim 0.63 \text{ min}^{-1}$, respectively. The median values and ranges of v_e were N1, 0.32 and $0.29\sim 0.70$; N2, 0.39 and $0.32\sim 0.60$; N3, 0.40 and $0.24\sim 0.62$, respectively.

 TABLE 2: The perfusion parameters of metastatic nodes among N staging ($n = 26$).

N stage	K^{trans} (min^{-1})	k_{ep} (min^{-1})	v_e
N1 ($n = 3$)	0.24 (0.17~0.26)	0.44 (0.33~0.66)	0.32 (0.29~0.70)
N2 ($n = 17$)	0.29 (0.17~0.46)	0.38 (0.13~0.67)	0.39 (0.32~0.60)
N3 ($n = 6$)	0.46 (0.29~0.70)	0.36 (0.10~0.63)	0.40 (0.24~0.62)

node were not correlated with N stage ($P = 0.485$ and 0.113 , resp.). The median values and ranges of k_{ep} were N1, 0.44 min^{-1} and $0.33\sim 0.66 \text{ min}^{-1}$; N2, 0.38 min^{-1} and $0.13\sim 0.67 \text{ min}^{-1}$; N3, 0.36 min^{-1} and $0.10\sim 0.63 \text{ min}^{-1}$, respectively. The median values and ranges of v_e were N1, 0.32 and $0.29\sim 0.70$; N2, 0.39 and $0.32\sim 0.60$; N3, 0.40 and $0.24\sim 0.62$, respectively (Table 2).

The mean values and ranges of K^{trans} , k_{ep} , and v_e in the primary tumors were 0.27 min^{-1} and $0.16\sim 0.48 \text{ min}^{-1}$; 0.62 min^{-1} and $0.25\sim 1.06 \text{ min}^{-1}$; 0.37 and $0.25\sim 0.60$, respectively. Using Spearman's correlation, none of the three DCE-MRI parameters in nodes were significantly correlated with the corresponding parameters in the primary tumors: for


 FIGURE 1: Box plots showing significant difference of K^{trans} in metastatic nodes by Kruskal-Wallis test among N staging ($P = 0.015$).

K^{trans} , $r = 0.224$ and $P = 0.272$; for k_{ep} , $r = 0.134$ and $P = 0.515$; for v_e , $r = 0.177$ and $P = 0.387$ (Figure 2).

4. Discussion

In this study, we evaluated the correlation between the DCE-MRI parameters in the metastatic lymph nodes and tumor N stage. Studies have been performed to compare the DCE-MRI parameters in lymph nodes that were confirmed to be positive and negative for malignancy by histology [15, 16]. Such studies have showed that malignant nodes have higher vascularity and microvessel permeability compared to benign nodes. Similarly, our findings also support the hypothesis that increased vascular permeability reflected by K^{trans} in metastatic lymph nodes is positively correlated with N stage; that is, the higher the N stage, which is an indicator of aggressiveness and portends poorer prognosis [4, 17], the higher the K^{trans} , which reflects higher permeability and perfusion. Such significant correlation should not be due to the nodal size, since the correlation between these perfusion parameters and nodal size was insignificant. It is widely accepted that these perfusion and permeability characteristics reflected by DCE-MRI are directly related to the tumor angiogenic activity [18–20] and that tumor N staging reflects the spread and extent of lymph node metastasis [10]. Based on the fact that angiogenesis is required to support cancer growth and metastasis, our results may be explained by the fact that nodes with more angiogenesis facilitate the spread of cancer cells in lymph node chains leading to a higher N stage.

We did not observe any significant difference in v_e or k_{ep} among tumors of different N stages. The k_{ep} , calculated as K^{trans}/v_e , is not an independent parameter; v_e is the measurement of volume of EES per unit volume of tissue and reflects the available space for contrast permeability. The lack of significance in the difference between v_e may indicate that the higher K^{trans} may be due mainly to the increased blood flow (perfusion) but not the EES volume, and that the increase

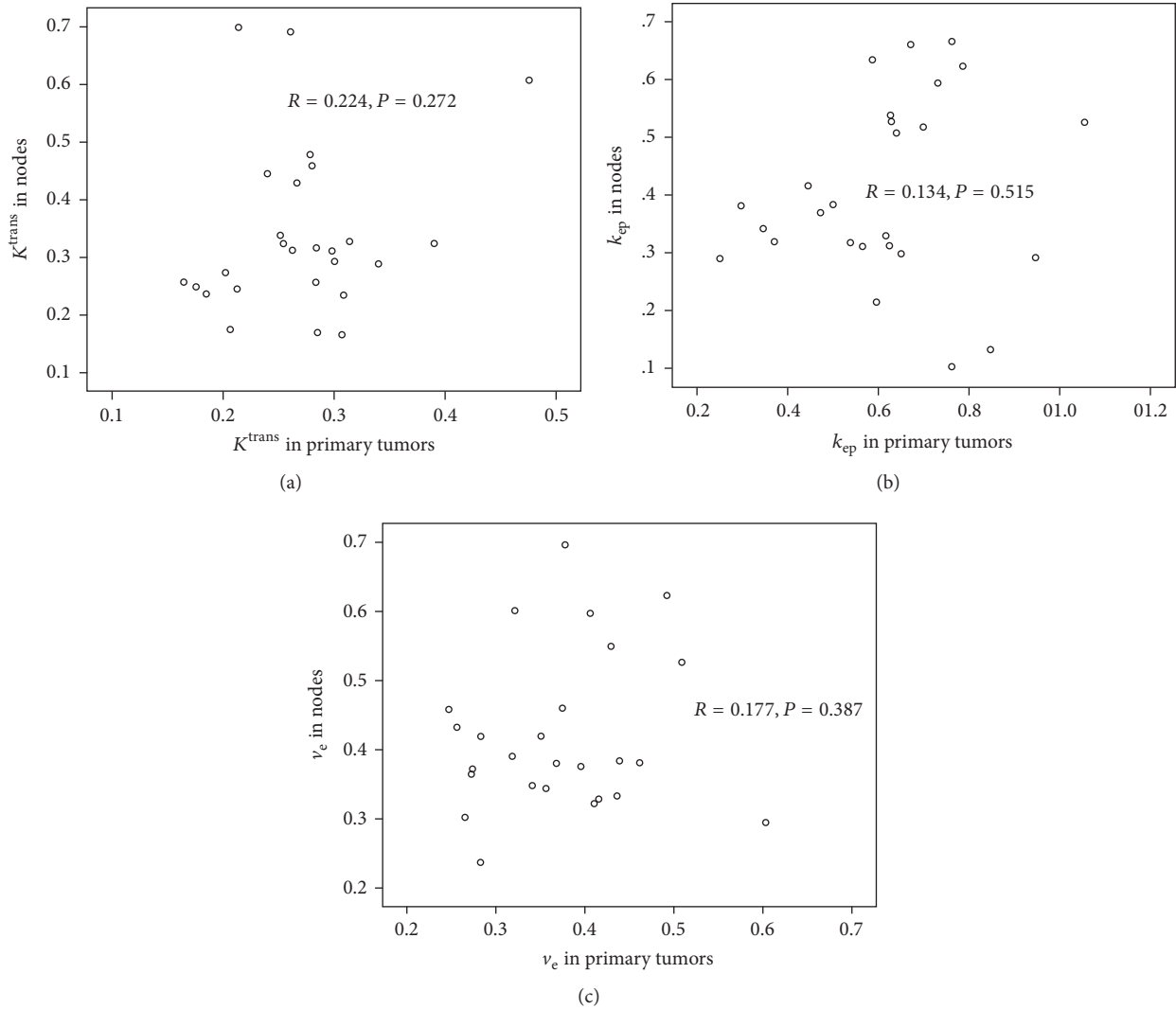


FIGURE 2: Scatter plots show no significant correlations between the DCE-MRI parameters in metastatic nodes and in primary tumors by Spearman's correlation: (a) K^{trans} ; (b) k_{ep} ; (c) v_e .

in K^{trans} may precede the increase in EES volume. Further prospective studies are required to confirm this finding.

The present study found that the DCE-MRI parameters in nodes were not significantly correlated with the corresponding parameters in primary tumors, similar to another study performed in cervical cancers and its nodal metastases [8]. This suggests that the tumor microvessel environment, that is, perfusion and vascular permeability, in the primary NPC tumor is independent of the characteristics in its metastatic lymph nodes. Thus, tumors with high perfusion and vascular permeability may neither develop nodal metastasis nor have more metastatic nodes. This discrepant finding between the primary tumor and its metastasis suggests heterogeneity that is intermetastatic and supports the notion that the metastasizing process of a malignant primary tumor may be related to genetic alterations in the primary tumor, which may be heterogeneous in nature [21, 22]. The primary tumor may release

a number of cells into the circulation; however only a small fraction of these cells establish metastases in a favourable organ or node in a nondeterministic manner [23]. Thereafter, continual evolution of the primary tumor reflects local selective advantages rather than future selective advantages, and thus growth at metastatic sites is not dependent on additional genetic alterations in the primary tumor. Such discrepancy between metastatic nodes and primary tumor indicates that attention should also be needed to the study of the metastases.

The results of our study, although the mechanism of which is still unclear, may have some clinical implications for clinical management of NPC patients. Since the perfusion parameters in nodes, but not in primary lesion, were significantly correlated with the tumor N stage, clinicians may pay more attention to these parameters in metastatic nodes due to the fact that N staging is critical in prognosis. On the other hand, one may expect to evaluate the role of such perfusion

parameters, which reflect the functional activity in tumors and metastatic nodes, in NPC patient management in the future studies.

Our study has some limitations. Firstly, the MRI scan coverage included the primary tumor and upper neck but not the entire neck. Thus, some regional metastatic lymph nodes may not have been included. However, it has been reported that lymph node metastasis generally spreads from the upper neck to the lower neck [24–26]; therefore the first lymph node station of spread is in the locoregional node adjacent to the primary tumor. Secondly, there may be an element of error in the placement of the ROI, as this procedure was completed manually, although accuracy was improved by confirming the location of the ROIs on the coregistered conventional T2W images.

5. Conclusion

In a cohort of new NPC patients, we found that perfusion and permeability based on DCE-MRI are higher in regional nodes of higher N stage tumors, and that the parameters in the nodes have no relationship with the corresponding parameters in its primary tumor. These findings showed that DCE-MRI in the metastatic lymph plays a distinct role in characterizing the nodal status in NPC. This finding, if further verified, may have important impact in the staging and management of NPC patients with metastatic lymph nodes.

Abbreviations

NPC:	Nasopharyngeal carcinoma
TNM:	Tumor-node-metastasis
EES:	Extravascular extracellular space
AJCC:	The American Joint Committee on Cancer
FOV:	Field of view
FFE:	Fast field echo
T2W:	T ₂ -weighted
B1MAP:	B1 mapping
FA15:	Flip angle of 15°
ROI:	Regions of interest.

Conflicts of Interest

The authors declare that they have no conflicts of interest.

Acknowledgments

This study is supported by Hong Kong Research Grants Council Areas of Excellence Scheme (no. AoE M-06/08) and The National Natural Science Foundation of China (no. 81301273).

References

- [1] M. Agulnik and L. L. Siu, “State-of-the-art management of nasopharyngeal carcinoma: current and future directions,” *British Journal of Cancer*, vol. 92, no. 5, pp. 799–806, 2005.
- [2] D. T. T. Chua, J. S. T. Sham, W. I. Wei, W.-K. Ho, and G. K. H. Au, “The predictive value of the 1997 American Joint Committee on Cancer stage classification in determining failure patterns in nasopharyngeal carcinoma,” *Cancer*, vol. 92, no. 11, pp. 2845–2855, 2001.
- [3] W. I. Wei and V. W. K. Mok, “The management of neck metastases in nasopharyngeal cancer,” *Current Opinion in Otolaryngology and Head and Neck Surgery*, vol. 15, no. 2, pp. 99–102, 2007.
- [4] L. Han, S.-J. Lin, J.-J. Pan et al., “Prognostic factors of 305 nasopharyngeal carcinoma patients treated with intensity-modulated radiotherapy,” *Chinese Journal of Cancer*, vol. 29, no. 2, pp. 145–150, 2010.
- [5] P. S. Tofts, G. Brix, D. L. Buckley et al., “Estimating kinetic parameters from dynamic contrast-enhanced T1-weighted MRI of a diffusable tracer: standardized quantities and symbols,” *Journal of Magnetic Resonance Imaging*, vol. 10, no. 3, pp. 223–232, 1999.
- [6] M. Sumi and T. Nakamura, “Extranodal spread in the neck: MRI detection on the basis of pixel-based time-signal intensity curve analysis,” *Journal of Magnetic Resonance Imaging*, vol. 33, no. 4, pp. 830–838, 2011.
- [7] N. Bhooshan, M. L. Giger, S. A. Jansen, H. Li, L. Lan, and G. M. Newstead, “Cancerous breast lesions on dynamic contrast-enhanced MR images: computerized characterization for image-based prognostic markers,” *Radiology*, vol. 254, no. 3, pp. 680–690, 2010.
- [8] N. J. Fischbein, S. M. Noworolski, R. G. Henry, M. J. Kaplan, W. P. Dillon, and S. J. Nelson, “Assessment of metastatic cervical adenopathy using dynamic contrast-enhanced MR imaging,” *American Journal of Neuroradiology*, vol. 24, no. 3, pp. 301–311, 2003.
- [9] B. Huang, C.-S. Wong, B. Whitcher et al., “Dynamic contrast-enhanced magnetic resonance imaging for characterising nasopharyngeal carcinoma: comparison of semiquantitative and quantitative parameters and correlation with tumour stage,” *European Radiology*, vol. 23, no. 6, pp. 1495–1502, 2013.
- [10] S. B. B. Edge, C. C. Compton, A. G. Fritz et al., *AJCC Cancer Staging Manual*, vol. 7, Springer, New York, NY, USA, 2010.
- [11] B. Whitcher and V. J. Schmid, “Quantitative analysis of dynamic contrast-enhanced and diffusion-weighted magnetic resonance imaging for oncology in R,” *Journal of Statistical Software*, vol. 44, no. 5, pp. 1–29, 2011.
- [12] J. F. Jansen, H. Schoder, N. Y. Lee et al., “Tumor metabolism and perfusion in head and neck squamous cell carcinoma: pretreatment multimodality imaging with 1H magnetic resonance spectroscopy, dynamic contrast-enhanced MRI, and FDG-PET,” *International Journal of Radiation Oncology*Biological*Physics*, vol. 82, no. 1, pp. 299–307, 2012.
- [13] S. Chawla, S. Kim, L. A. Loevner et al., “Prediction of disease-free survival in patients with squamous cell carcinomas of the head and neck using dynamic contrast-enhanced MR imaging,” *American Journal of Neuroradiology*, vol. 32, no. 4, pp. 778–784, 2011.
- [14] S. Kim, L. A. Loevner, H. Quon et al., “Prediction of response to chemoradiation therapy in squamous cell carcinomas of the head and neck using dynamic contrast-enhanced MR imaging,” *American Journal of Neuroradiology*, vol. 31, no. 2, pp. 262–268, 2010.
- [15] K. A. Kvistad, J. Rydland, H.-B. Smethurst, S. Lundgren, H. E. Fjøsne, and O. Haraldseth, “Axillary lymph node metastases in breast cancer: preoperative detection with dynamic contrast-enhanced MRI,” *European Radiology*, vol. 10, no. 9, pp. 1464–1471, 2000.

- [16] C. M. Wendl, S. Müller, J. Meier et al., "High resolution contrast-enhanced ultrasound and 3-tesla dynamic contrast-enhanced magnetic resonance imaging for the preoperative characterization of cervical lymph nodes: first results," *Clinical Hemorheology and Microcirculation*, vol. 52, no. 2–4, pp. 153–166, 2012.
- [17] M. Jun, L. Liu, L. Tang et al., "Retropharyngeal lymph node metastasis in nasopharyngeal carcinoma: prognostic value and staging categories," *Clinical Cancer Research*, vol. 13, no. 5, pp. 1445–1452, 2007.
- [18] A. Steingoetter, D. Menne, and R. F. Braren, "Assessing antiangiogenic therapy response by DCE-MRI: development of a physiology driven multi-compartment model using population pharmacometrics," *PLoS ONE*, vol. 6, no. 10, Article ID e26366, 2011.
- [19] S. J. Ahn, C. S. An, W. S. Koom, H.-T. Song, and J.-S. Suh, "Correlations of 3T DCE-MRI quantitative parameters with microvessel density in a human-colorectal-cancer xenograft mouse model," *Korean Journal of Radiology*, vol. 12, no. 6, pp. 722–730, 2011.
- [20] M. L. George, A. S. K. Dzik-Jurasz, A. R. Padhani et al., "Non-invasive methods of assessing angiogenesis and their value in predicting response to treatment in colorectal cancer," *British Journal of Surgery*, vol. 88, no. 12, pp. 1628–1636, 2001.
- [21] R. Bernards and R. A. Weinberg, "A progression puzzle," *Nature*, vol. 418, no. 6900, article 823, 2002.
- [22] R. S. Kerbel, "Growth dominance of the metastatic cancer cell: cellular and molecular aspects," *Advances in Cancer Research*, vol. 55, pp. 87–132, 1990.
- [23] M. Yu, S. Stott, M. Toner, S. Maheswaran, and D. A. Haber, "Circulating tumor cells: approaches to isolation and characterization," *The Journal of Cell Biology*, vol. 192, no. 3, pp. 373–382, 2011.
- [24] W.-F. Li, Y. Sun, M. Chen et al., "Locoregional extension patterns of nasopharyngeal carcinoma and suggestions for clinical target volume delineation," *Chinese Journal of Cancer*, vol. 31, no. 12, pp. 579–587, 2012.
- [25] F. C. H. Ho, I. W. K. Tham, A. Earnest, K. M. Lee, and J. J. Lu, "Patterns of regional lymph node metastasis of nasopharyngeal carcinoma: a meta-analysis of clinical evidence," *BMC Cancer*, vol. 12, article 98, 2012.
- [26] A. D. King, A. T. Ahuja, S.-F. Leung et al., "Neck node metastases from nasopharyngeal carcinoma: MR imaging of patterns of disease," *Head and Neck*, vol. 22, no. 3, pp. 275–281, 2000.